The pore pressure regime of the northern Gulf of Mexico: Geostatistical estimation and regional controls

Scott Morris, Brian Vestal, Kelsey O'Neill, Michael Moretti, Cesar Franco, Nathan Hitchings, Jianmin Zhang, and John D. Grace

ABSTRACT

Subsurface pressures strongly influence the migration and trapping of hydrocarbons and impact the safety and efficiency of drilling operations. The pore pressure field of the northern Gulf of Mexico (GOM) was analyzed at 1000-ft (305-m) depth intervals from 2500 to 17,500 ft (762 to 5334 m) below the sea floor. Two variables were mapped: 12,976 initial hydrocarbon reservoir pressure gradient values and 43,276 observations on drilling fluid (mud) weight. Because of the acute importance of assessing estimate uncertainty, ordinary kriging was employed, providing explicit evaluations of confidence surrounding mapped values. Expected values and confidence intervals for the distribution of both variables were estimated by 9 mi² (23.3 km²) grid cells across the GOM for each of the 15 depth intervals. Estimation variances were also used to clip each map to specific extents, within which a uniform minimum threshold of certainty was exceeded.

Characteristic of young basins with high sedimentation rates, mean pore pressure exceeded hydrostatic pressure throughout the GOM. Four provinces of internally consistent pressure regimes were defined: three south of Louisiana and one off the Texas coast. They reflect geologic controls on pressure arising from regional patterns of sedimentation and the resultant timing and geometry of salt tectonism. One GOM-wide (shallow) vertical transition in the pressure field was found in the mud weight data, and a second vertical transition (deep) occurred in both variables. Hot spot analysis was also applied to identify specific contiguous areas of abnormally high or low rates of change in pressure gradient and mud weight between depth-adjacent intervals.

Copyright ©2015. The American Association of Petroleum Geologists. All rights reserved.

Manuscript received August 13, 2013; provisional acceptance January 10, 2014; revised manuscript received April 10, 2014; final acceptance July 22, 2014.

DOI: 10.1306/07221413148

AUTHORS

SCOTT MORRIS ~ Earth Science Associates, 4300 Long Beach Blvd., Ste. 310, Long Beach, CA 90807; scott@earthsci.com

Scott Morris earned his bachelor's degree in statistics from the University of California, Riverside and his master's degree in applied mathematics from California State University, Fullerton. He is currently working at Earth Science Associates where he handles various predictive analytics focusing on log-linear regression.

BRIAN VESTAL ~ University of Colorado, Anschutz Medical Campus, Colorado School of Public Health, Department of Biostatistics and Informatics, Aurora, CO 80045; brian.e.vestal@ gmail.com

Brian Vestal is currently a doctoral candidate in the department of biostatistics and informatics at the University of Colorado Anschutz Medical Campus. His most recent research involves developing new methods for quantitative medical image analysis using a spatial point process framework.

KELSEY O'NEILL ~ Earth Science Associates, 4300 Long Beach Blvd., Ste. 310, Long Beach, CA 90807; kelsey@earthsci.com

Kelsey O'Neill earned a B.S. degree in geography and environmental studies from Florida State University in 2010, and is currently working toward a M.Sc. Degree in predictive analytics from Northwestern University. She performs geotechnical research and analysis at Earth Science Associates.

MICHAEL MORETTI ~ Mathematics Department, California State University, Fullerton, 154 McCarthy Hall, Fullerton, CA 92834; michael. moretti@csu.fullerton.edu

Michael Moretti earned his B.S. degree in mathematics from the University of La Verne. He continued his education at California State University, Fullerton, receiving a master's degree in applied mathematics. He is currently an instructor in the Department of Mathematics, California State University, Fullerton.

CESAR FRANCO ~ Farmers Insurance Group, Corporate Actuarial Department, 4700 Wilshire Blvd., Los Angeles, CA 90010; cfranco87.cf@ gmail.com

Cesar Franco graduated from the California State University, Fullerton with a bachelor's degree in mathematics in 2010 and a master's degree in applied mathematics in 2012. He is presently employed as an actuary in the Corporate Actuarial Department of the Farmers Insurance Group.

NATHAN HITCHINGS ~ Pac Comm Technologies, Inc., 4430 E. Miraloma Ave., Suite A, Anaheim, CA 92807; nathan.hitchings@gmail.com

Nathan Hitchings received bachelor's and master's degrees in applied mathematics from California State University, Fullerton. He is now lead mobile engineer at Tikr.

JIANMIN ZHANG ~ Mathematics Department, California State University, Fullerton, 154 McCarthy Hall, Fullerton, CA 92834; jmzhanq01@yahoo.com

Jianmin Zhang received her B.S. degree in applied meteorology from the Nanjing Institute of Meteorology, M.S. degree in applied meteorology from the Chinese Academy of Meteorological Sciences, Ph.D. from the University of Minnesota, Twin Cities in soil science and master's degree in applied mathematics from California State University, Fullerton.

JOHN D. GRACE ~ Earth Science Associates, 4300 Long Beach Blvd., Ste. 310, Long Beach, CA 90807; john@earthsci.com

John D. Grace is president of Earth Science Associates. He received his Ph.D. in economics from Louisiana State University. He joined ARCO's R&D lab in 1985 as a research geologist, became a manager in geologic research and subsequently in corporate planning before founding ESA in 1991. His focus has been in resource assessment, basin analysis, quantitative solution of geologic problems, and developing GIS as an analytic tool. He has taught geology and applied mathematics at LSU, University of Southern California, and California State University, Fullerton, where he directed the seminar that produced this study.

ACKNOWLEDGEMENTS

This study is principally the product of the 2012 capstone research seminar for master's candidates in applied mathematics at California State University, Fullerton. The authors wish to thank Earth Science Associates for financial support and access to their software. We greatly benefited from the guidance of Tim Coburn, Tony Dupont, Bill Gearhart, Jim Kalinec, Sam Mentemeier, John Snedden, and Harold Syms on an early draft of this paper. We also appreciate the very careful reviews and comments of the *Bulletin* Editor, Michael Sweet, and two anonymous reviewers on the originally submitted manuscript, which greatly improved the final paper.

INTRODUCTION

The distribution of pore pressures within a sedimentary basin plays a critical role in the localization of hydrocarbons and impacts the safety and efficiency of drilling operations. For the former, analysis has centered on modeling the flow of fluids in response to stresses applied to them during burial; these models may be local or regional. For the latter purpose, studies are typically local, exploiting the experience in neighboring wells and using seismic data and/or well logs to predict pressure ahead of drilling a specific target.

Our analysis takes a different approach, estimating regional pressure based on geostatistical (kriging) analysis of very large databases of initial reservoir pressures and drilling mud weights. A geostatistical approach was chosen because it allows the user to explicitly assess the certainty and statistical support for the values mapped. Because of the operational implications of pore pressure in drilling safety and to demonstrate the value of incorporating probability in geologic mapping, uncertainty was represented unambiguously throughout the analysis.

The geostatistical method provided two scales of information on reliability. Locally, for any point at which mud weight or initial reservoir pressure gradient was mapped, a confidence interval (here 10%/90%) was supplied. Globally, the mapped geographic extent for each variable was clipped by a single statistical information criterion for blanking. This regional, probabilistic analysis supplements but does not replace either process modeling or the use of geophysical data for pore pressure prediction (PPP).

The analysis was applied to the pore pressure field in the northern Gulf of Mexico (GOM) (Figure 1). The GOM is one of the world's most active provinces for the exploration and production of oil and gas. By late 2012, in federal waters, 52,346 wells had been drilled and about 1440 fields discovered. The estimated ultimate recovery of the fields in the region as of December 31, 2007 was 53.3 billion barrels of oil equivalent (BOE), of which 86% had been produced (BOEM, 2011).

The basic analytic results on the GOM pressure field were summarized in maps of estimated pressure gradient and mud weight for each of fifteen 1000 ft (305 m) depth intervals. Each map was clipped by a uniform rule on statistical certainty so no inferences about the pressure field would be made beyond the areas of empirical support. The interval maps were also processed to produce an estimate, throughout the GOM, of the depth to the top of hard geopressure (0.7 psi/ft [15.8 kPa/m]), a commonly used datum in pressure analysis. Variations in the depth to the top of hard geopressure very clearly reflect division of the GOM pressure field into four large and internally consistent regions.

Derivative analysis of the pressure gradient maps produced two final results: (1) identification of hot spots (rock volumes with anomalously high or low vertical rates of change in pressure) and (2) vertical transition zones, in which the spatial continuity of the pressure field changed significantly. Comparative analysis of the two variables in depth also identified areas in which there were systematic

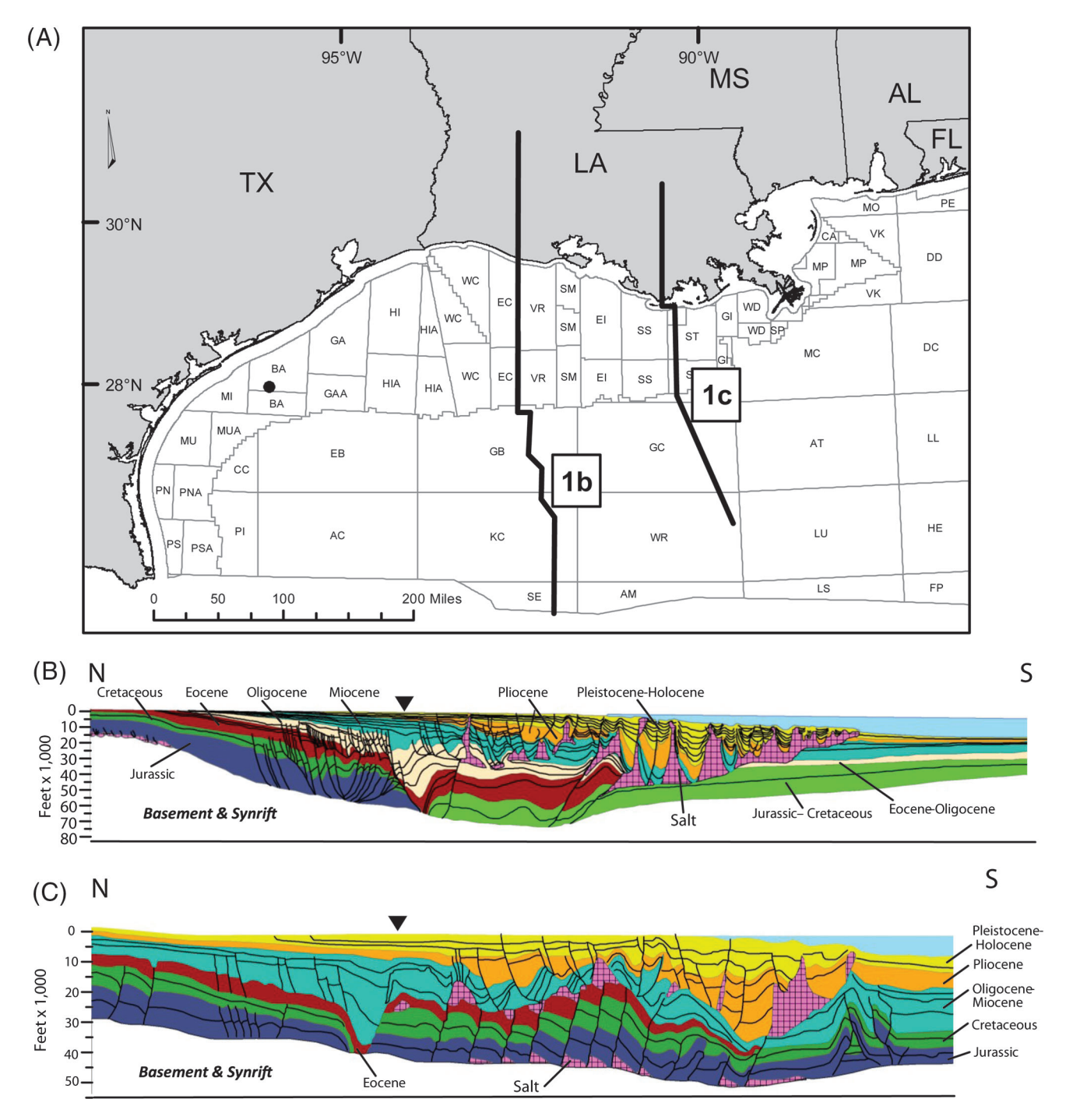


Figure 1. The locations (A) of the regional cross sections (B and C) and the location of the Brazos 22A field referenced in Figure 7 (the black dot). The licensing protraction areas of the Gulf of Mexico are shown with name abbreviations referenced in the text. Stratigraphic cross sections (B and C) are modified from Peel et al. (1995), with permission from AAPG. The cross sections are vertically exaggerated by a factor of 5, and the inverted triangle at the top of each indicates the location of the coast.

differences between the results for the pressure gradient and mud weights.

The methods of pore pressure analysis employed here were designed to be transparent and specifically to enable others to explicitly change the criteria of acceptable certainty and such designations as hot spot or transition zone to meet their own analytic needs. They also represent methodological innovations that highlight both the role of statistical certainty in mapping analytic results and focus on horizontal and vertical gradients within a field variable (pressure). The specific findings for the GOM drew strong relationships between the distribution of pore pressures and broad geologic controls related to sediment accumulation rate and salt tectonics.

RESEARCH CONTEXT

Pore Pressure Prediction

In a hydrostatic regime, the pressures of fluids in sedimentary rock pores increase linearly with depth. In the GOM, assuming formation waters contain dissolved solids of 100,000 parts per million, the normal rate of increase is 0.465 psi/ft (10.52 kPa/m). However, several mechanisms can create pressure gradients greater than the hydrostatic norm: sedimentation rates high enough to prevent pressure equilibration between pores as overburden stress is applied (compaction disequilibrium); fluid or sediment compressibility; local fluid expansion due to clay diagenesis; hydrocarbon generation, migration, and in situ conversion of oil to gas; ambient temperature; changes in overburden density; and tectonic stresses. Locally, the rate of increase in pressure with depth can also reverse as a result of opposite relative changes in the same factors.

Although pressure plays a large role in hydrocarbon migration and trapping, it is of urgent importance because drilling in areas with unanticipated changes in pressure can produce dangerous and costly effects. Because of this, considerable research has been invested in PPP. The principal directions have been (1) process modeling of fluid flows within sediments resulting from burial and (2) extraction of pressure information from geophysical data.

Mathematical models of fluid and sediment responses to burial began in one vertical dimension (Sharp, 1976) and extended to two dimensions for analysis of groundwater movement, petroleum migration, and ore genesis (Bethke, 1985). This foundation was further extended to 2.5-D or pseudo threedimensional (3-D) modeling, then to full simultaneous treatment of flow and the factors causing it in three spatial dimensions (Throndsen and Wangen, 1998). Finally, 3-D process analysis, when inputs change in time steps, produces four-dimensional estimates of the evolution of fluid flow and pressure in a rock volume over geologic time. These are typically deterministic, finite element models based on physical laws where rock/fluid properties and local geologic history have been discretized into 3-D cells of fixed sizes.

The use of seismic data for PPP developed along several lines, most tracing back to the empirical observation and the principle that seismic velocity through overpressured intervals declines relative to depth. Where overpressure arises because of compaction disequilibrium, porosity at a given depth is greater than normal compaction implies. This raises the share of bulk rock volume composed of fluid/gas-filled pores, which transmit sound at a slower velocity than the surrounding rock matrix. Therefore, where overpressure preserves more porosity than normal compaction, transit velocity drops.

Improving the accuracy and resolution of seismic-based PPP has focused on changing standard seismic processing to preserve and enhance pressuresensitive attributes (Sayers et al., 2002) and on improving seismic calibration with local well logs, vertical seismic profiles, and core analyses of seismic velocities. These improvements increase the vertical resolution of formation features and identify anisotropies that signal abnormal pressures (Carcione and Helle, 2002). Analyses of attributes beyond interval compressional-wave velocity (e.g., amplitude-offset data [Louie and Asad, 1994]) and exploitation of shear-wave components (Dvorkin et al., 1999) have also evolved. To this suite, potential field data have added an orthogonal approach to PPP, independent of the limitations of seismic techniques tied to the velocity-pressure relationship (Huffman, 2002).

Data from several well logging tools have been employed for PPP including bulk density, neutron porosity, sonic, and resistivity data. From some tools, the porosities associated with a normal compaction curve are computed, and log-derived empirical deviations from that curve are inferred as evidence of overpressure (Henning et al., 2002). While usually effective at identifying anomalous pressures due to compaction disequilibrium—the most common cause of overpressure in young, poorly consolidated rocks—they are not always sensitive to other mechanisms causing overpressure (e.g., fluid expansion) (Law and Spencer, 1998).

For PPP using both seismic and well log data, two important innovations have occurred principally in the last decade. First was the development of the ability to record both seismic and petrophysical data in real time while drilling (measurement while drilling, MWD). Second is the evolution of software that takes both pre-drill and MWD data and processes them for timely prediction of changes in pressure before they are encountered by the drill bit. Pressure indications derived directly from drilling performance itself (through analysis of weight on bit, torque, and the corresponding rates of rotation and penetration) can supplement geophysically based PPP (Lesso and Burgess, 1986). Reducing the risk of pressure-driven drilling hazards has immediately motivated these technologies.

In parallel with these advances, tighter integration of regional process modeling with local seismic and well log data has produced better regional- and prospect-level PPP, not only to forecast drilling hazards but to better model hydrocarbon migration and evaluate seal competence.

This study adds analysis from tens of thousands of wells and thousands of reservoirs for a strong, empirical regional foundation for further improvement by the type of methods referenced above. It also provides depth-specific refinement of regional modeling for fluid flows from 2-D and 3-D burial history models.

Previous Mapping of GOM Pressure

In an onshore band within 35 to 75 mi (56 to 121 km) of the coast of the Gulf of Mexico, starting in the 1930s as wells began to regularly exceed depths greater than 9000–10,000 ft (2743–3048 m), drillers

began to increasingly encounter downhole pressures exceeding hydrostatic pressure. This prompted research to understand why these conditions arose and to estimate the lateral and vertical dimensions of abnormal pressures. In an early contribution, Dickenson (1953) employed direct measurements, well tests, and production data to obtain downhole pressures and supplemented these with mud weights as a pressure proxy. He recognized the bias in mud weight (see subsequent text) and reduced the pressures they implied by a uniform 10%, noting that this factor was rough and lacked a broad empirical foundation. Dickenson focused on identifying the geologic conditions associated with or causing geopressure including depth and juxtaposition of thick sand and shale units, isolated sands encased within thick shales, and in sands otherwise hydrodynamically isolated by sealing faults and/or facies change with the loss of permeability.

Dickenson gave a graphic correlation between pressure and depth, with a low boundary established by the hydrostatic gradient (0.465 psi/ft [10.49 kPa/m]) and a high boundary drawn at the estimated overburden pressure (1.0 psi/ft [22.57 kPa/m]). In his map, covering only onshore south Louisiana, he spotted the locations of wells encountering abnormal pressure and biostratigraphically assigned the depth of their first occurrence with the age of the formation penetrated at that point. Dickenson defined abnormal very conservatively as any pressure gradient that exceeded hydrostatic.

Dickenson made no attempt to exactly interpolate the depth to top of abnormal pressure regionally, only drawing the boundaries between the geologic ages in which shallowest geopressure occurred. This map does, however, show that moving south through south Louisiana to the coast, the age of the section at which abnormal pressures occurred becomes progressively younger, with age-unit boundaries running roughly parallel with the modern coast.

By the 1970s, focus on geopressure extended to harnessing the potential energy in fluids exceeding hydrostatic (and the thermal energy and dissolved methane they also contained). Several scientists at the US Geological Survey (USGS) assessed geopressure and geothermal resources nationally (Muffler, 1979). As part of that effort, Wallace et al. (1979)

collected pressure data from government and company sources for onshore and offshore wells. Their data (including 1362 offshore wells) were divided into fourteen 1500 ft (457 m) depth cohorts. They included pressures tests, mud weight, well log header data, and electric log interpretation. Wallace et al. (1979) estimated pressure gradients within each well and assigned linearly interpolated pressure to depth cohort midpoints.

Research by Burke et al. (2012) concluded that to contour the depth to the 0.7 psi/ft (15.8 kPa/m) gradient isoline, Wallace et al. (1979) probably used a form of local polynomial interpolation. This is a deterministic gridding algorithm that conformably smooths a surface through the areas between observations using neighboring control points to determine the local parameters for the user-determined degree of a two-dimensional polynomial globally representing the surface. Because of data constraints of that time, Wallace et al. (1979) were only able to map offshore to approximately 300 ft (91 m) of water depth.

In a methodologically similar approach, almost 30 yr later, a new group of USGS scientists mapped the depth to iso-pressure gradients from 0.6 through 1.0 psi/ft by 1.0 psi/ft intervals (13.5 through 22.6 kPa/m by 2.25. kPa/m intervals) for the northern half of the Gulf of Mexico basin, both offshore and onshore (Burke et al., 2012). Their principal attention centered on the depth to the 0.7 psi/ft (15.8 kPa/m) gradient. The source of almost all their data was a proprietary database of about 200,000 mud weight observations from approximately 70,000 wells across the northern basin; about 2500 of these were offshore. The (positive) bias in mud weight-estimated pressure was recognized and given an average value of 0.03 psi/ft (0.67 kPa/m) by the authors, but their data were not corrected by this factor (see subsequent text).

Like Wallace et al. (1979), Burke and colleagues estimated the pressure gradients vertically within individual wells by linear interpolation of intra-well pressure as a function of depth. By deriving pressure gradients from mud weights, Burke et al. (2012) implicitly used mean sea level as a reference datum for depth in calculation of the pressure per foot (i.e., the gradient). However, when mapping depth to the top of an iso-gradient (e.g., 0.7 psi/ft) offshore,

Burke et al. (2012) used the seafloor as zero depth (and, correspondingly, land elevation above mean sea level onshore). With irregularly spaced estimated depths to 0.7 psi/ft (15.8 kPa/m) in hand for each well, they gridded and contoured their observations with a more flexible variant of the local polynomial interpolation used by Wallace et al. (1979).

Dickenson's work did not extend offshore, but he found key two regularities in the spatial distribution of abnormal pressures that extend offshore: (1) a transition from normal to abnormal pressure begins at about 9000 to 10,000 ft (2743 to 3048 m) below mean sea level, and (2) coincident with regional stratigraphy, this transition zone passes through younger rocks basinward. The present study reaffirms these conclusions.

Generalizing the work of Wallace et al. (1979) leads to conclusions that also agree well with the present study: south of the Louisiana coast, the depth to the 0.7 psi/ft (15.8 kPa/m) iso-gradient is deep (fitting within the Louisiana Inner Shelf region [see subsequent text]). This surface shallows further to the south, but because of the limitations on extant data, their surface only coincides with the northern-most part of the Louisiana Outer Shelf region and does not extend into the Deep Water region at all. On the Texas shelf, the same relative increase in lateral heterogeneity was observed. Throughout the areas common to both Wallace et al. (1979) and the present study, there are many areas of fine-scale disagreement, most probably related to differences in data density and gridding.

The Burke et al. (2012) map of depth to the 0.7 psi/ft (15.8 kPa/m) iso-gradient below seafloor is comparable to the results of this study and of very similar areal extent offshore. The regional results are strikingly similar. Three differences separate the two analyses of depth to the top of the 0.7 psi/ft (15.8 kPa/m) iso-gradient: (1) The present study used approximately six times more wells for mud weight observations, and cell size used here is half the area used in the Burke et al. (2012) study. As a result of this and the gridding method, there is much finer local detail presented here. (2) Because the authors mentioned previously all used deterministic gridding algorithms to predict variable values between control points, there is no assessment of the statistical certainty underlying the mapped values. (3) Because of the

imposition of a certainty-based clipping rule in the present study, mapped results in this study do not extend beyond a consistently defined distance from controls. In the Burke et al. (2012) map, extrapolation extends up to approximately 35 mi (56.3 km) from controls with no guidance on the reliability of those estimates of depth to iso-pressure gradient contours.

Regional Geologic Development

To set the regional geologic context, the basin's opening in the mid-Jurassic established three fundamental features that dominated the controls on the present regional distribution of pressure. (1) A stable, roughly circular synclinal structure is centered halfway between the southern tip of Florida and Mexico. This produced persistent regional dips: on the northwestern margin (along the south Texas coast), down to the east; rotating clockwise along the coast, the dip shifts to the southeast; and, finally, due south on the northern margin (around the Mississippi River delta). (2) After the basin opening, a widely distributed, variable-thickness (Louann) salt was deposited across the study area during the Late Jurassic. (3) Subsequently, and perhaps most importantly, the northwestern and northern basin margins became the terminal sedimentary catchment for erosion over what is today almost one-quarter of the North American landmass.

Most of the Cenozoic sedimentary fill in the study area is associated with four continent-scale phases of crustal uplift during which the northwestern and northern margins have prograded 150 to 180 mi (240 to 290 km) toward the basin center (Galloway et al., 2000). The corresponding principal axes of sediment transport moved from western and northwestern provenance through the Paleocene to an intermediate position in the early Miocene. Thereafter, sediments were sourced broadly from the north, from across what is now the central United States, entering the gulf through the greater Mississippi river system.

Because of the lateral switching of the large sediment pulses, its episodic nature, local accumulation rates in the Cenozoic varied greatly throughout the study area (Snedden et al., 2013). These ranged from nondeposition and low rates favoring small grain

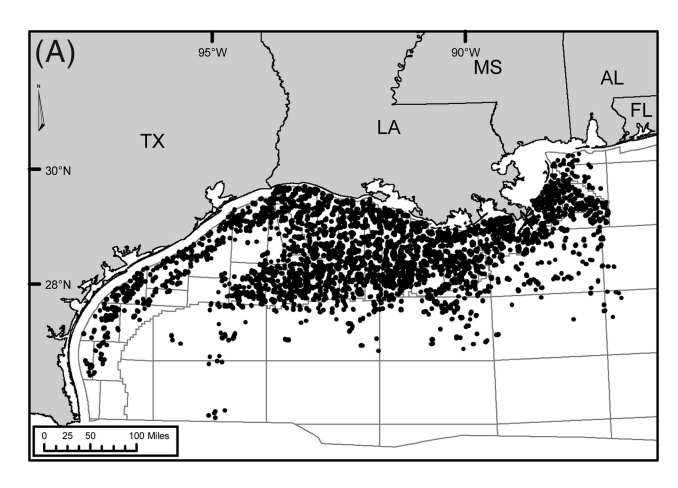
sizes to massive dumps of coarse-grain material, with concomitant listric faulting and basement accommodation. This progradation vertically mobilized the Louann Salt and during Pliocene–Pleistocene sediment accumulation rate highs, also transported salt downdip, over younger sections, toward the basin center (see Figure 1B). Within this period of active and variable sedimentation, the Gulf of Mexico basin became a world-class hydrocarbon province.

This history produced local and regional hydrodynamic compartments within and between which the free flow of fluids and gases was pervasively impeded, vertically and laterally, almost completely preventing preservation of a hydrostatic pressure gradient anywhere in the study area. Allochthonous salt, in part, perhaps, dependent on its local geometry, alternately provided vertical pathways for equilibrating fluid flow or obstructed those flows. Moreover, vertical and lateral emplacement of salt (and its corresponding withdrawal from its sources) created a widespread rugosity relative to margin-wide dips that further hampered fluid flow. Variations in sand-shale ratios and sealing faults, in addition to trapping hydrocarbons, confined fluids generally and promoted the maintenance of pressures above hydrostatic. Hydrocarbons themselves (and their phase transitions) have also contributed to local pressure highs.

DATA

Two types of data on pore pressure were employed in this study: initial pressures in oil and gas reservoirs and mud weight from drilling records. Both data sets were taken from Earth Science Associates' GOM³ system as of November 2012 (Earth Science Associates, 2012). These observations were based on data provided by operators through the US federal agencies managing offshore mineral development: the Bureau of Ocean Energy Management (BOEM formerly the Minerals Management Service [MMS]) and the Bureau of Safety and Environmental Enforcement (BSEE). The locations of observations from both data sets are shown in Figure 2. All raw data in the study are directly available from BSEE (BSEE, 2012).

From the pressure observations, pressure gradients were calculated by dividing the observed



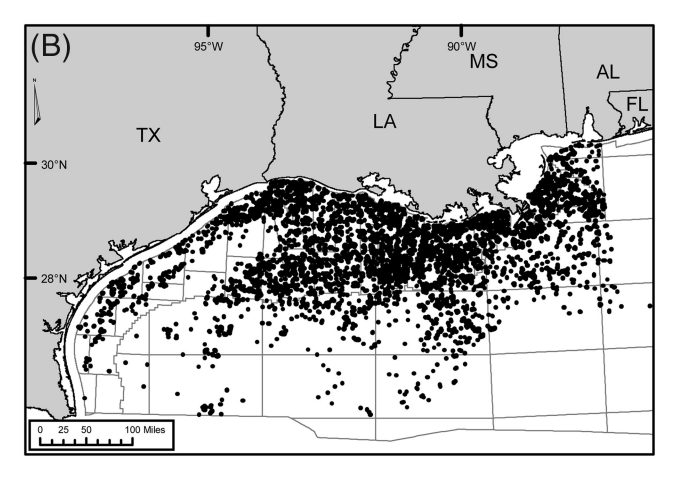


Figure 2. Locations of observations for initial reservoir pressure gradient (A) and mud weight (B).

pressure by the reservoir's total vertical depth in feet below mean sea level and are measured in psi/ft (kPa/m) (Minerals Management Service, 2001). Mud weight observations come from well operator's reports filed with the United States government and are recorded in pounds per gallon (ppg) (grams per cubic centimeter, g/cc). After elimination of obvious outliers, 12,976 observations on pressure gradient and 43,276 observations on mud weight were used in the study. Analysis of initial reservoir pressure gradients and mud weights were kept separate in the study, although the results were compared. Initial reservoir pressure gradient is derived from a direct measurement of pressure made for a specific depth.

Mud weight systematically reflects pressures anticipated over drilling intervals. However, considerations of engineering strategy enter drillers' mud programs. Engineers may weight-up mud so it intentionally exceeds the empirical pressure over a depth interval. Often, mud weight higher than necessary is used as a safety factor. Additionally, considerations of formation damage by mud invasion of rock, rock fracturing, drilling speed, and various components of drilling cost are included in determining a mud program, conflating singular consideration of pressure at depth.

In order to investigate the variation in pressure gradient and mud weight with depth, both data sets were divided into 1000 ft (305 m) depth intervals. Following industry practice, these intervals were referenced to the sea floor (mud line) (Appendix 1).

Intervals with sufficient data for analysis extended from 2500 ft below the mud line (ftbml) (762 meters below the mud line, mbml) to 17,500 ftbml (5639 mbml), divided into 15 intervals. Summary statistics on the pressure gradient are shown in Table 1 (with all tables, in Appendix 2) and Figure 3A and for mud data in Table 2 and Figure 3B.

METHODOLOGY

A key advantage of kriging models for gridding spatially distributed variables is that in addition to producing a mappable value, they provide information on the uncertainty surrounding those mapped values. By treating the value of a variable at every point on the map as a distribution of possible values, two critical statistics emerge for each grid cell in a kriged map. First is the mathematically expected value, which is the mean of the distribution of possible values for a cell. This is the central tendency of that distribution and is the best estimate for the value of the variable at that location (Figure 4A). Second is the variance of the distribution of possible values for a cell, reflecting the relationship between the estimated (mean) value of the variable and the probability that its true value occurs within a specific range. This is represented by the kriging standard error (KSE) (Figure 4B). The higher the KSE for a grid cell, the greater the uncertainty surrounding the mapped mean value and the wider the interval within which

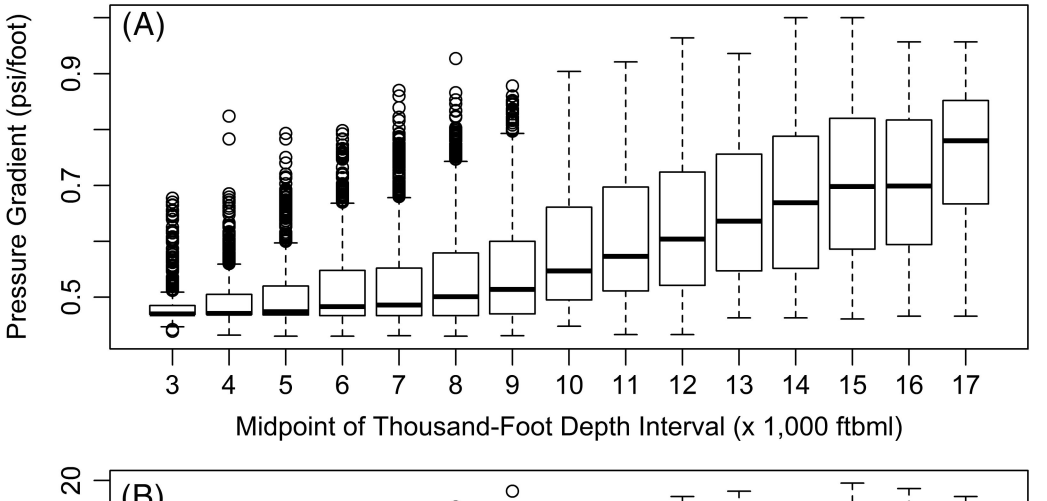
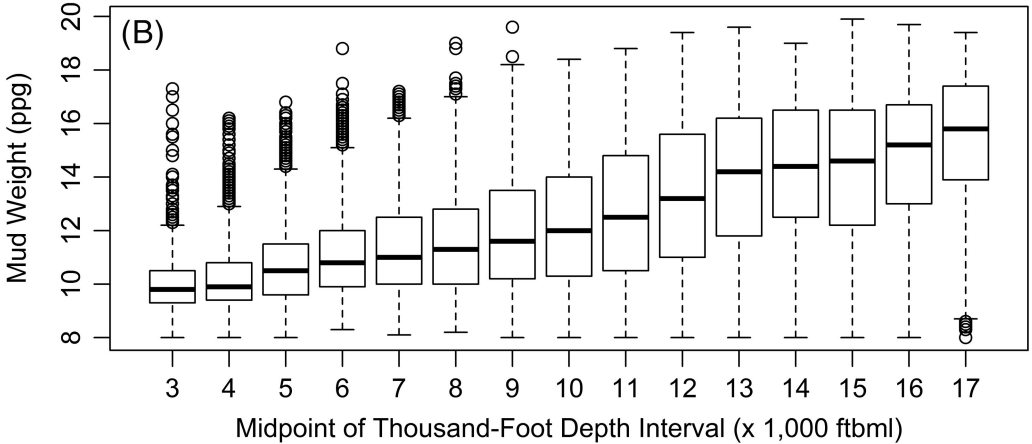


Figure 3. The statistical distributions of pressure gradient data (A) and mud weight data (B) by intervals used in the study. The dark black lines in the boxes are median values; the boundaries of the boxes represent the top of the first and third quartiles of the distributions, respectively; the length of the whiskers are set at 1.5 times the interquartile range, and the dots represent outliers in the distributions.



the true value is expected to fall with a given probability.

Estimating Pressure Gradient and Mud Weight

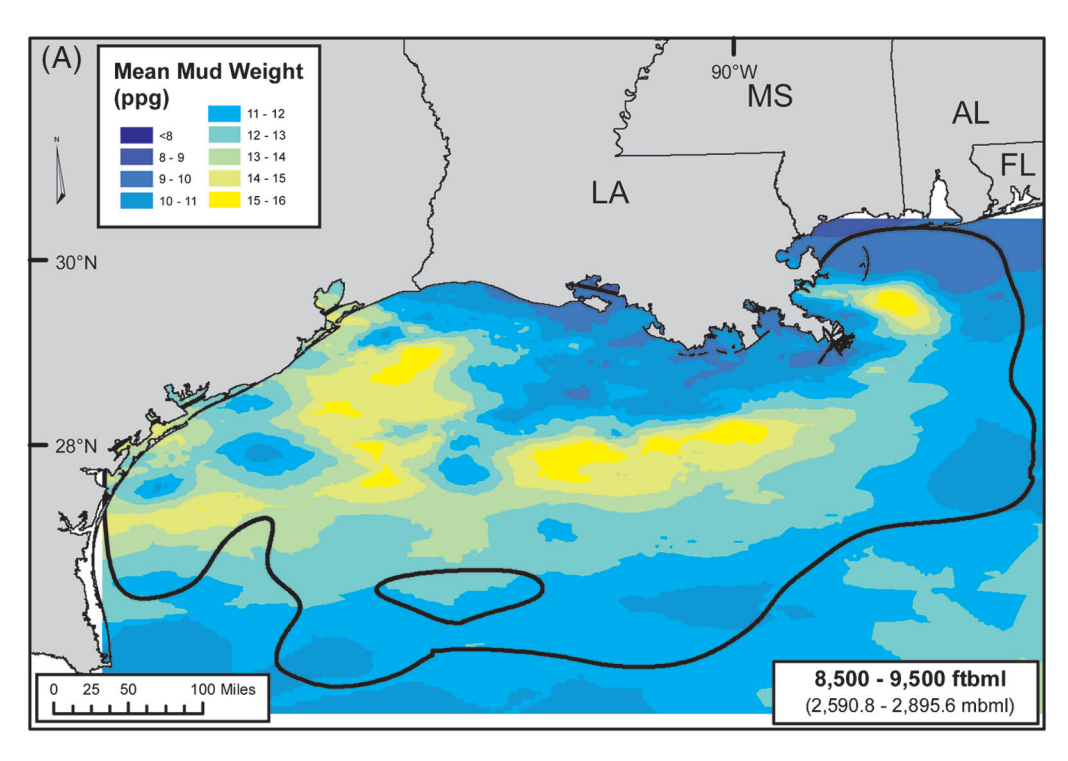
To estimate the initial reservoir pressure gradient and mud weight for each depth interval across the study area, ordinary kriging, as implemented in the Geostatistical Analyst extension to ArcGIS 10.0 by Esri, was applied (for general methodology, see Isaaks and Srivastava, 1989; for software, see Johnston et al., 2001). All data for both variables was similarly projected (Universal Transverse Mercator, tile UTM15N with the NAD 1927 datum) in maps sharing a common rectangular extent and cell size (9 mi² [23.3 km²]), which corresponds roughly to the size of most US Gulf of Mexico lease blocks). Final maps for both the pressure gradient and mud weight have standard and comparable legends.

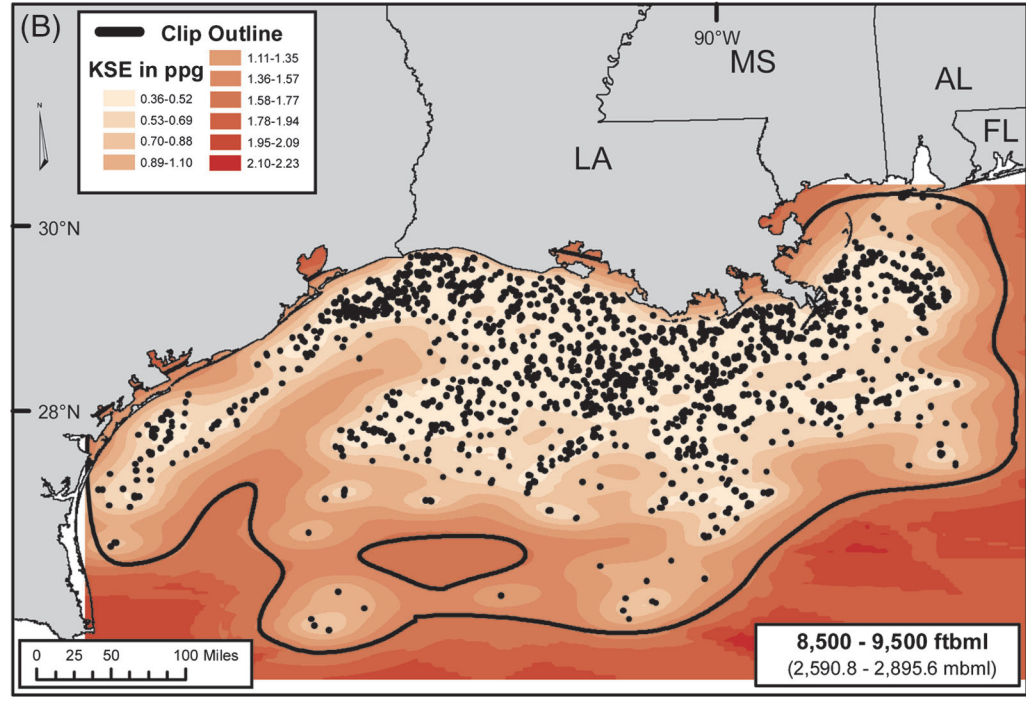
Kriging is a very flexible interpolator that can handle a wide range of situations given suitable choices made in the parameters and proper processing of the data. Before performing ordinary kriging, the data was detrended using a second-order global polynomial that was estimated using an exponential kernel. This helps justify the assumption of stationarity needed for ordinary kriging, and a second-order global polynomial was chosen because it captures the bowl-shaped geometry of the half-basin-synclinal shape of the Gulf Coast basin without over fitting the data. Also, since the data is grouped by 1000 ft (305 m) depth interval cohorts, it is possible to have two or more data points with the same exact latitude and longitude in the same depth interval. In such cases, the points were averaged and treated as a single observation for the remainder of the kriging procedure.

The semivariograms were estimated using the stable model, a generalization of the exponential. All

99

Figure 4. Estimated mud weight (in ppg) (A) and kriging standard error (KSE, in ppg) (B) for the 8500-9500 ftbml (2590.8-2895.6 mbml) depth interval mapped with its original rectangular extent. The black lines on both show where the mud weight map (A) was ultimately cropped to exclude areas of the original rectangular extent where the value of KSE exceeded the minimum certainty criteria. The black dots in (B) locate the mud weight observations used for this depth interval.





models used 12 distance cohorts (lags) to bin the data separation distance and 45° angular bins to accommodate anisotropy. The lag size was estimated independently of each interval using the Geostatistical Analyst built-in optimization. In most cases, the lag size calculated by Geostatistical

Analyst seemed reasonable with a few exceptions. For these, several lag sizes were compared, and the lag size with the lowest root mean squared error (RMSE) was chosen to be used instead. Once the lag size was set, the parameters of the model (shape, nugget, and partial sill) were calculated by

Geostatistical Analyst. These parameters, as well as the number of observations (obs) used for each model, can be found in Tables 3 and 4 (Appendix 2).

Once the semivariograms were estimated, the search neighborhood was defined to determine which points of control would be used in the estimation of each cell. The search neighborhood used the major/ minor range and angle of anisotropy estimated from the semivariogram and was defined to have four sectors with a 45° offset to ensure points of control were used from every direction. A maximum of five and a minimum of two of the nearest neighbors in each sector were used to make each estimate. Maps of the pressure gradient and mud weights were then calculated for each depth interval, as well as corresponding maps of the KSE. Statistics on the results of these analyses for both variables for all 15 depth intervals are shown in Tables 5 and 6 (Appendix 2). As an example, the mud weight and KSE maps for the 8500-9500 ftbml (2590.8–2895.6 mbml) interval are shown in Figure 4.

Analysis of Uncertainties

Three types of estimation uncertainty information can be extracted to analyze pressure at different scales. At local and regional scales, maps of estimated pressure gradient and mud weight are paired with their respective KSE map (as in Figure 4). The KSE maps provide critical context to the information in the pressure gradient and mud weight maps, showing the rate and anisotropic way in which variance, therefore, uncertainty increases as a function of distance and direction from control.

The second measure was designed to assess uncertainty at a local scale, for individual grid cells in the map. Using the estimated value and KSE, a confidence interval surrounding the predicted value for each cell was produced (equation 1). This mirrors the construction of confidence intervals used in classical (nonspatial) statistics. We assume a normal distribution so the 10%/90% (80%) confidence interval (CI) is defined as

$$CI_{80} = \hat{Z}(s_0) \pm \alpha_{80}, \quad \alpha_{80} = 1.282(KSE)$$
 (1)

where $\hat{Z}(s_0)$ is the estimated value for pressure gradient/mud weight in a single cell, and 1.282 is the score from a standard normal table associated with an 80% probability. Interpreted, this means that if repeated samples were taken, 80% of the time the confidence intervals calculated will contain the true value of $Z(s_0)$.

Using Figure 5 as an example, there are three steps to determine the confidence interval at any point in a map:

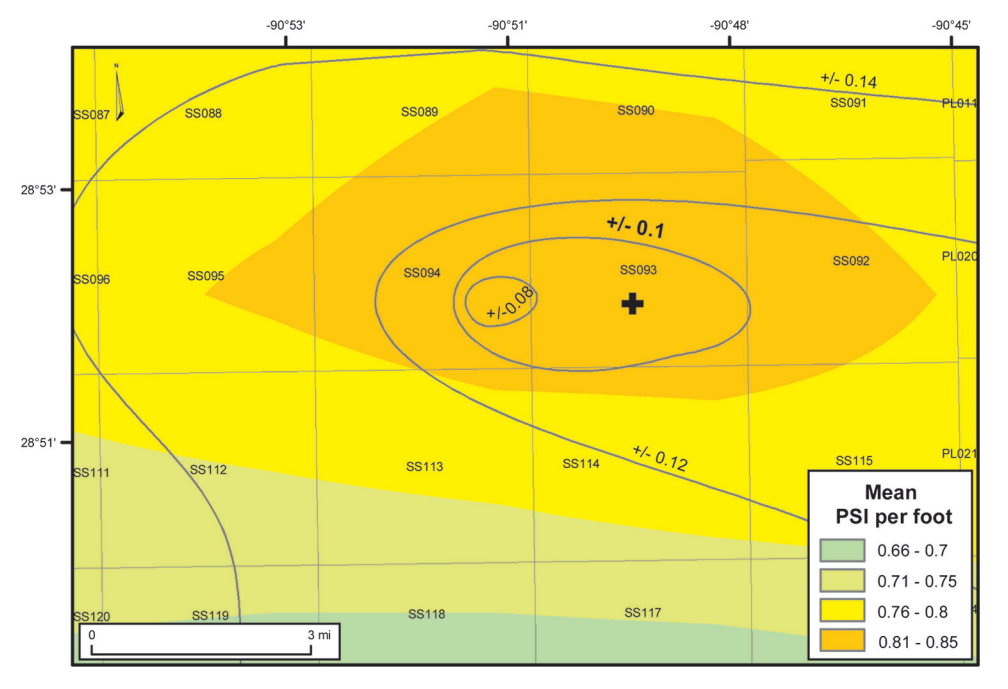


Figure 5. Predicted reservoir initial pressure gradient for the 12,500-13,500 ftbml (3810-4115 mbml) depth interval and contoured confidence interval information. At the black cross. the estimated pressure gradient (read from the color and the midpoint of the legend category) is 0.83 psi/ft (18.8 kPa/m), and the nearest enclosing CI contour line (bold) is ± 0.1 psi/ft (2.3 kPa/m). The labeled square cells are lease blocks in the Ship Shoal (SS) protraction area of the Gulf of Mexico (see Figure 1A for the location of the SS area).

- 1. Determine the estimated (mean) value of the pressure gradient at a point from the color of the map and the legend.
- 2. Find the closest enclosing contour line, which is labeled with the value of α_{80} .
- 3. Add and subtract the value of α_{80} to and from the estimated mean value to yield the 10%/90% CIs.

Finally, at a global scale, the mapped extent was limited to those areas exceeding a uniform minimum level of certainty. The original maps share a common rectangular extent with dimensions determined by the geometric distribution of input data rather than by the reliability of the resultant analysis. Processed, the maps were clipped to the extent within which the spatial analysis, using kriging, added information beyond simply averaging data for a mean and applying a global variance as a measure of uncertainty. In Figures 4A and B, this limit is indicated by the black lines.

Typically the coefficient of variation or signal-tonoise ratio is used as a measure of uncertainty, but these statistics do not produce meaningful results for the methodology used in this study. Instead, a new ratio, the kriging standard ratio (KSR), was estimated and applied to each cell to decide if it met the confidence threshold. Two steps were involved.

 Compute the KSR for a cell, equal to the KSE for that cell (KSE_i) divided by a measure of global variance, the standard deviation of all of the data in that depth interval (σ):

$$KSR_i = \frac{KSE_i}{\sigma}$$

The KSE is a measure of uncertainty that considers the spatial variation of the data while the standard deviation is a measure of uncertainty that does not. Therefore, the closer KSR is to zero, the greater the reduction in uncertainty brought by spatial modeling as opposed to simple averaging. On the other hand, if KSR = 1, modeling the spatial process brought nothing to reduce uncertainty relative to a nonspatial computation of mean and standard deviation of the data.

2. For each map, determine the maximum $KSR_{max} = maximum(KSR_i)$. KSR_{max} represents the cell in which spatial analysis added the least

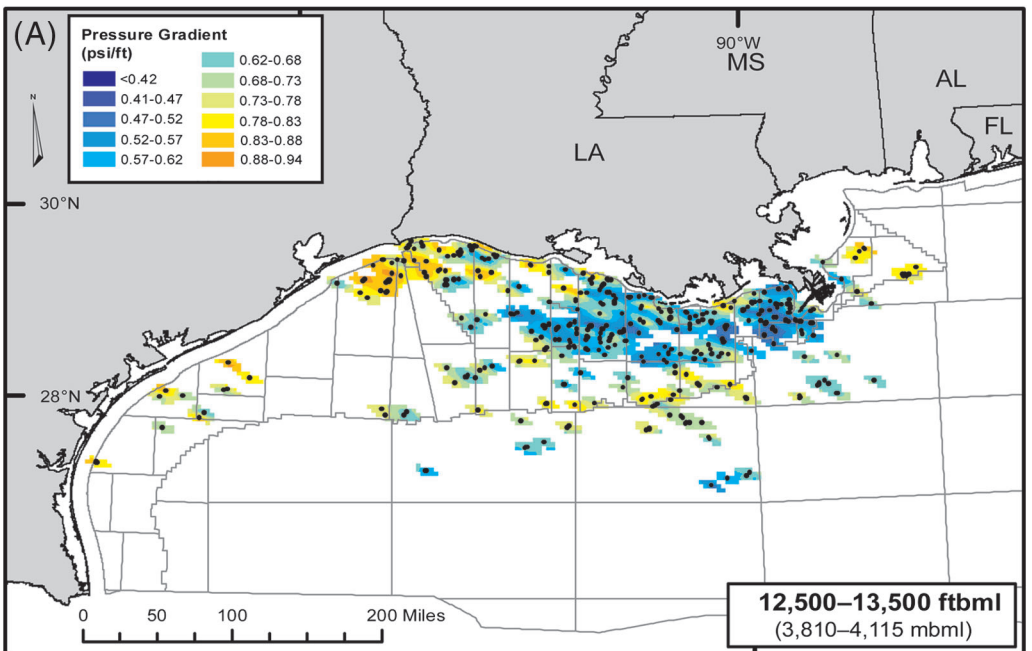
information relative to a nonspatial model. All cells in the map having a $KSR_i > 0.7(KSR_{max})$ were eliminated from the map (blanked).

A different threshold, stricter than 70% of (KSR_{max}) could be used. However, the 70% threshold produced tractable results and confirms a new methodology for representing uncertainty on a map that can be adjusted depending on the purposes to which the map will be put. In map view, the value of subjecting all maps to a threshold of minimum confidence is illustrated in Figure 6, and Figure 7 shows the influence of both the local and global uncertainty information at the Brazos 22A field as a function of depth.

Pressure Hot Spots

In addition to the maps of estimated mud weight and pressure gradient for the 15 depth intervals, the study extended to investigate changes in both variables as explicit functions of depth. For normally pressured rocks, the rates of increase with depth for both variables should be zero. The rocks below the GOM are not normally pressured, so the average rate of increase per 1000-ft (305-m) interval was empirically determined. Then, for each depth interval, actual changes in mud weight and pressure gradient in the corresponding cells of depth-adjacent intervals were analyzed to find abnormal areas, regions where pressure changed with depth at either a rate significantly greater or less than the interval-wide average rate. Areas of lower-than-average changes with depth include those areas where mud weight or pressure gradient actually declined between one 1000-ft (305-m) interval and the next deepest one.

Using mud weight as an example in Figure 8, the hot spot map (Figure 8B) was estimated by subtracting the estimated mud weight in each grid cell in the 9500–10,500 ftbml (2896–3200 mbml) interval (Figure 8A) from the estimated mud weight in the vertically corresponding cell of the 10,500–11,500 ftbml (3200–3505 mbml) interval (Figure 8C). This yielded a distribution of differences that closely followed a normal distribution, with a mean difference of 0.446 ppg (0.053 g/cc) and standard deviation of 0.814 ppg (0.098 g/cc). This allows



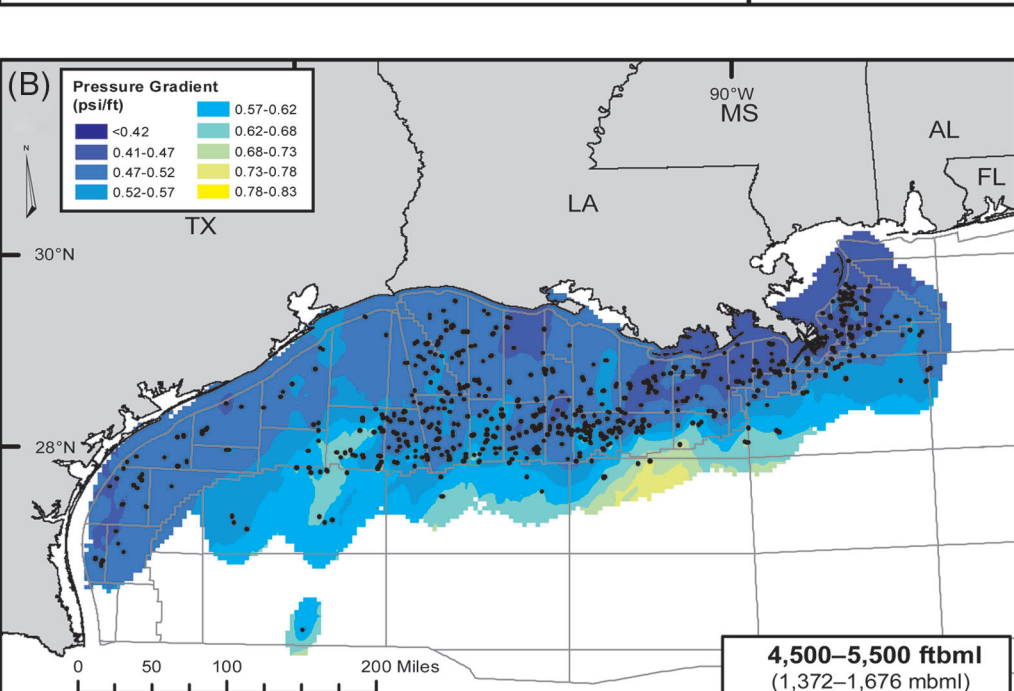


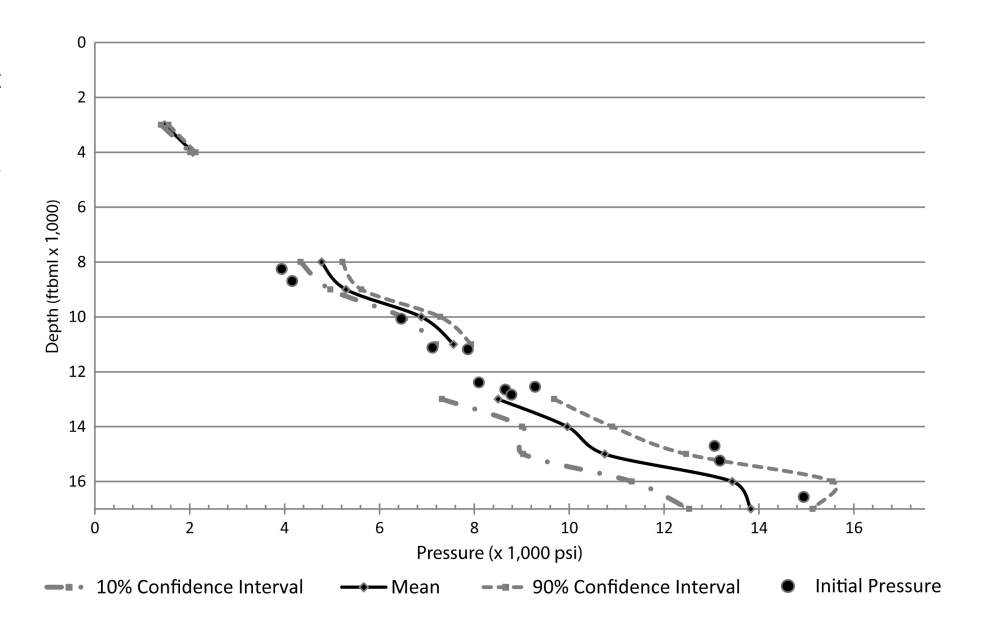
Figure 6. Comparison of the clipped extent of pressure gradient maps between two depth intervals. The extent of the 12,500-13,500 ftbml (3810-4115 mbml) interval (A) is very severely clipped because of extremely high spatial variance in the data (Table 3, Appendix 2). The 4500-5500 ftbml (1372-1676 mbml) interval (B) has lower spatial variance and supports interpolation and extrapolation farther from control than in the 12,500-13,500 ftbml (3810-4115 mbml) interval (A). This contrast between the intervals is also reflected in the crossvalidation RMSE as the RMSE for (B) is less than half of the RMSE for (A) (Table 5, Appendix 2). RMSE = root mean squared error.

the classification of cells into three categories: insignificant change in pressure, increasing pressure, and decreasing pressure.

A key finding from this analysis is that for both mud weight and pressure gradient, the spatial distribution of positive and negative anomalous areas is not random, that is, red, blue, and yellow cells are not randomly scattered across the map in Figure 8B. Instead, they form large, contiguous areas of positive and negative anomalies for both mud weight and pressure gradient. These results indicate significant regional differences in pressure regimes, probably reflecting large compartments in the sedimentary section, some of which extend over several thousand feet vertically.

To test the statistical significance of the clustering of positive and negative anomalies in Figure 8B, the Anselin Local Moran's I test was applied to

Figure 7. The relationship between predicted pressure and uncertainty at the Brazos 22A field. The estimated pressure (based on mud weight) is shown as a black line, surrounded by the 10%/90% confidence intervals (gray dashed lines). Also posted are the actual initial pressures for the BA 22A reservoirs (black dots). Gaps in the graph represent depth intervals clipped out at this location because local spatial variance exceeded the global confidence standard $(0.7[KSR_{max}])$ for each interval map. The location of the field is shown in Figure 1A.



identify significant contiguous anomalies (hot spots) (Anselin, 1995). These statistically significant positive and negative clusters for the difference in mud weight between the two intervals (Figure 8A and C) in Figure 8B are shown by thick red and blue polygons overlaid in the map. These polygons are also overlaid in Figure 8A and C for reference.

RESULTS

This study produced two types of results: direct and derivative. The direct results were reflected in the prediction and KSE maps for mud weight and reservoir initial pressure gradient over the GOM for the fifteen 1000 ft (305 m) depth intervals from 2500 to 17,500 ftbml (762 to 5334 mbml). These maps evidenced strong regional continuities in the pore pressure field, identifying four major regions of consistent pressure regimes. The investigation also identified areas and depths where changes in pressure were either anomalously high or low and where there was an unusually large vertical and/or lateral increase in spatial variability of the pressure field.

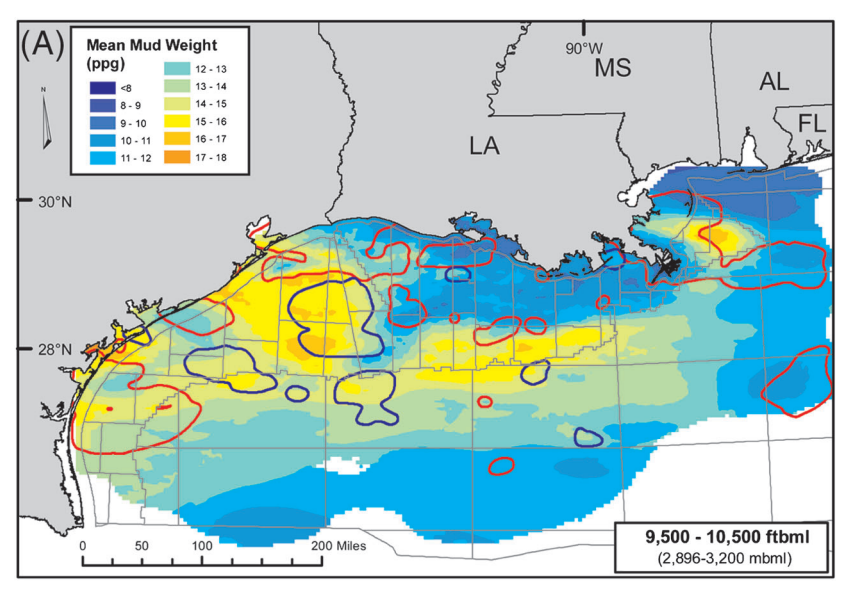
Classification of the GOM areally into broad pressure regime regions can be most easily seen in Figure 9A (plan view), 9B (3-D), and 9C (cross section). Figure 10A–N show the error-clipped maps of pressure gradient and mud weight for alternating depth intervals.

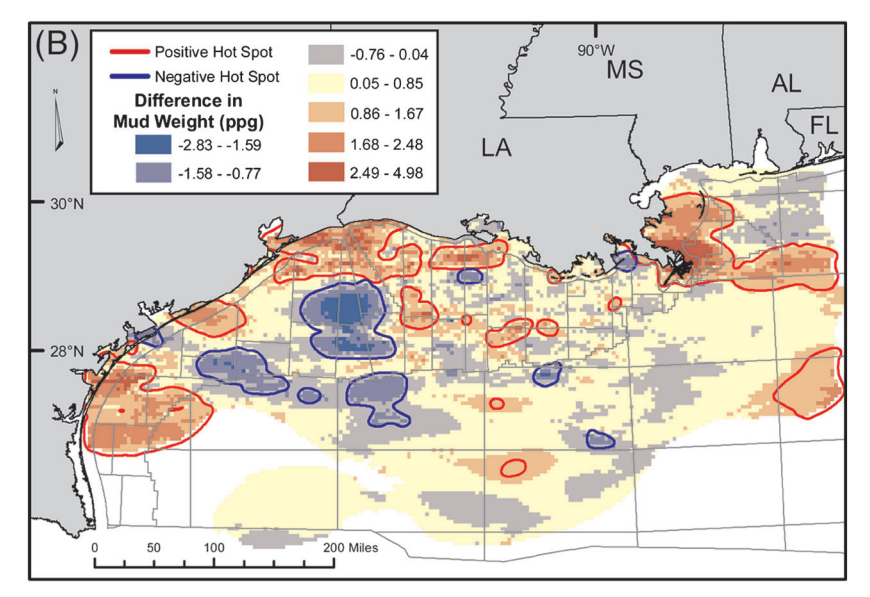
Regional Pressure Regimes

From the depth to the top of hard geopressure (Figure 9A), the regional pattern in the pressure field is very clear: seaward of the Louisiana coast, there is a low overpressure region; to its south is a high overpressure region parallel to the modern shelf-slope break and finally in Deep Water, another low overpressure region. The Texas shelf and slope are united into a region which, while relatively high overpressure, is best characterized by wide variability, laterally and vertically. These four areas appear to be broadly correlated with the timing, scale, and magnitude of sediment accumulation and with both the salt-tectonic and faulting responses to large sedimentary pulses and the hiatuses between them.

Louisiana Inner Shelf

Louisiana Inner Shelf is a region extending between 40 to 60 mi (64 to 97 km) south of the Louisiana coast from the modern Mississippi River delta, continuing approximately 200 mi (322 km) to the west (Figure 9A). This is a relatively low-pressure regime from the shallowest intervals through the 15,500–16,500 ftbml (4724–5029 mbml) interval. The average depth to the top of hard geopressure is 14,049 ftbml (4282 mbml) with a standard deviation of 1595 ft (486 m) and the shallowest hard geopressure is found in the 6500–7500 ftbml (1981–2286 mbml) interval.





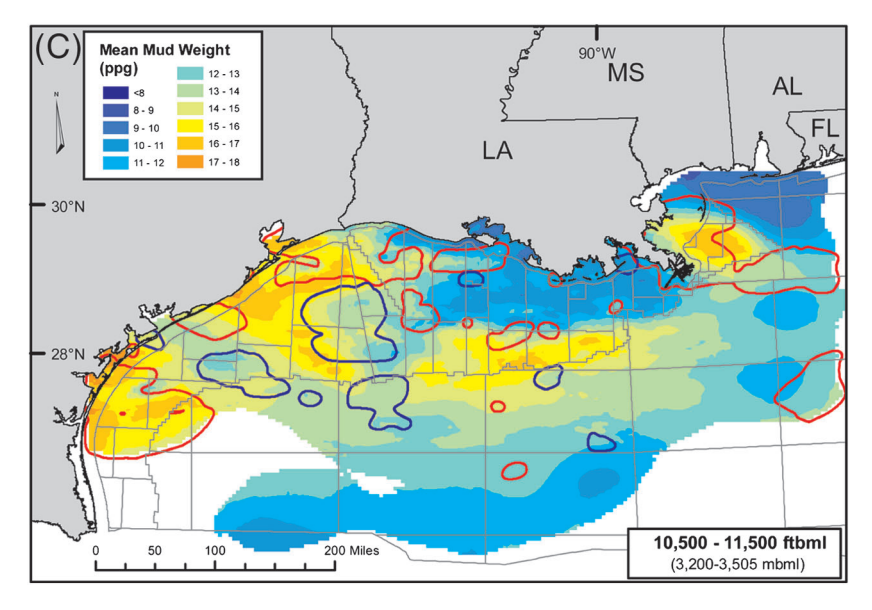
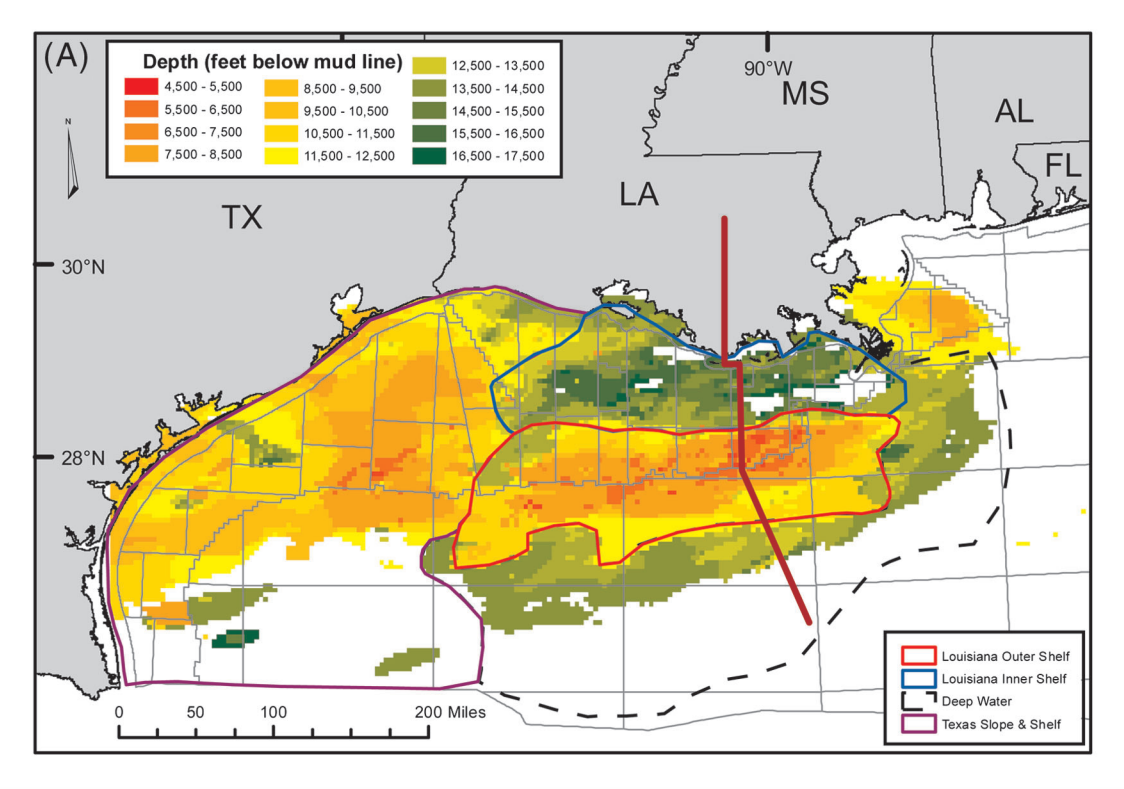
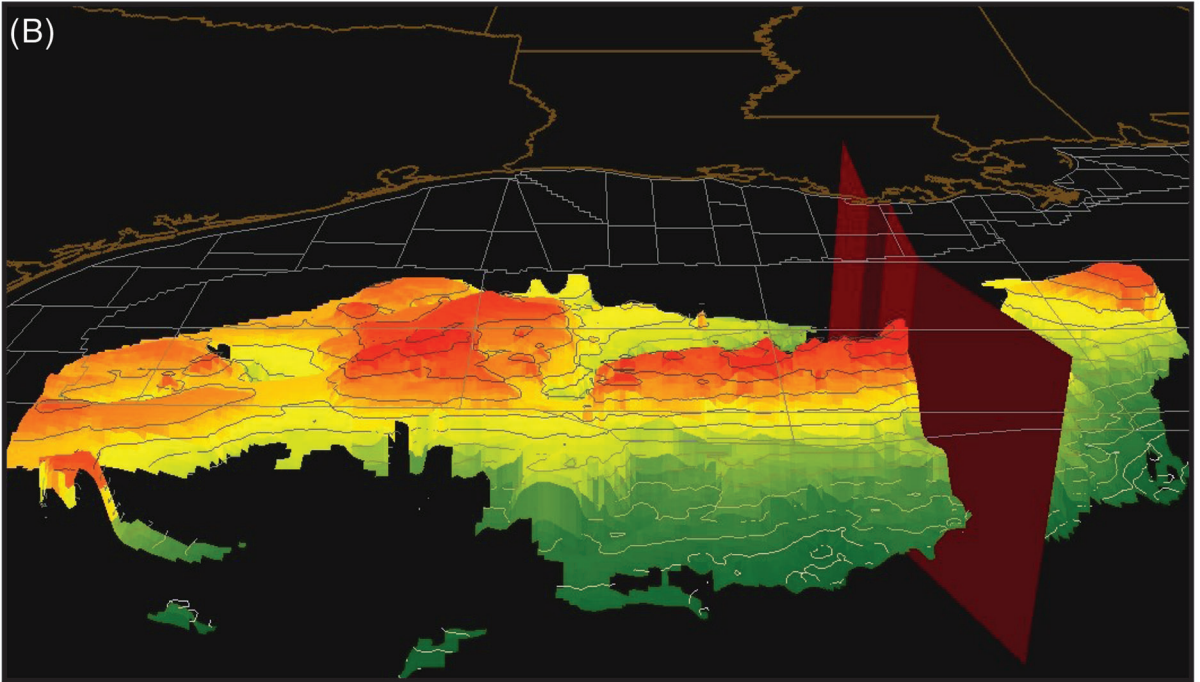
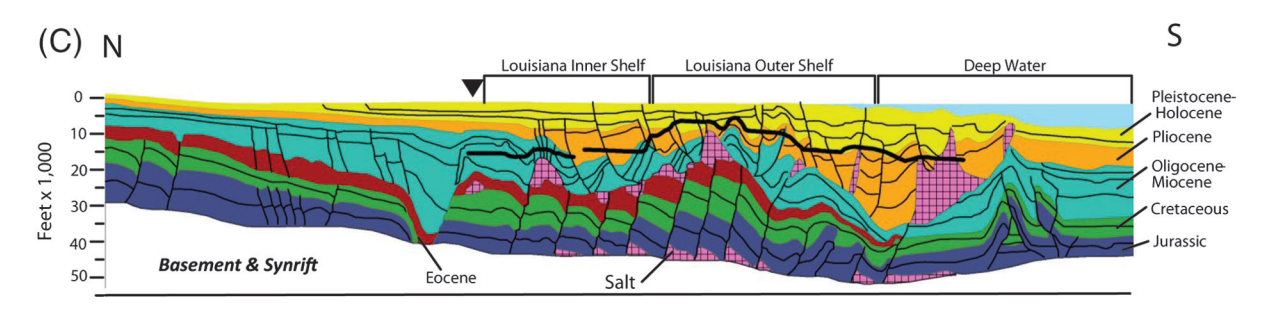


Figure 8. Results of the hot spot analysis of vertical changes in mud weight for two depthadjacent intervals. The estimated mud weight for the 9500-10,500 ftbml (2896-3200 mbml) interval (A) was subtracted from the estimated mud weight for the 10,500-11,500 ftbml (3200-3505 mbml) interval (C) to produce the difference map (B). Yellow indicates areas in (B) where the rate of increase in mud weight between the two intervals was within ± 0.5 standard deviations of the Gulf of Mexico-wide average difference between them. Blues indicate regions where the rate of increase in mud weight between the two intervals was less than 0.5 standard deviations of the Gulf of Mexicowide average between those intervals; reds indicate where the vertical rate of change was greater than 0.5 standard deviations of the Gulf of Mexico-wide average. The red polygons indicate statistically significant contiguous clusters of abnormally high rates of change in mud weight relative to the Gulf of Mexico-wide average between these two intervals and blue polygons indicate statistically significant clusters of abnormally low rates of change in mud weight. The red and blue polygons from (B) are repeated on the mud weight maps (A and C) to allow comparison of individual anomalous areas on the constituent interval mean mud weight maps.







Two important related regional features of the Louisiana Inner Shelf province may have contributed to the development of an extensive area of relatively low (i.e., closer to hydrostatic) pressure. First is the timing and magnitude of sedimentation. The highest sediment accumulation rate (SAR) occurred at the end of the late Miocene through the early Pliocene (Galloway et al., 2009). The maximum was moderate in magnitude, locally exceeding 4000 ft/m.y. (1219 m/m.y.) but across most of the region, less than the 1000–1500 ft/m.y. (305–457 m/m.y.) range.

Perhaps as important, since the regional SAR maximum in the late Miocene-early Pliocene, the largest sedimentary pulses have bypassed the Louisiana Inner Shelf region, depositing further to the south. This left the SAR in the region low (<1000 ft/m.y. [305 m/m.y.]) and relatively constant over the last 4 m.y. Over that period, SARs exceeding the average occurred (particularly in the south where the proximal end of the large depocenters above the lower Pliocene were occasionally located) but only in small areas (Snedden et al., 2013). Compounding the effect of a lower and temporally consistent SAR, with the Louisiana Inner Shelf in a more proximal position, a larger share of sediments deposited there would be coarser grained (than further south) with higher permeabilities that more readily equilibrate overpressured section.

Related to depositional history, the timing and gross morphology of salt tectonics differentiates the Louisiana Inner Shelf region from the two regions to the south. The period of greatest salt movement was coincident with the late Miocene—early Pliocene SAR maximum (Peel et al., 1995). However, subsequent structural growth of salt bodies during the slow and relatively uniform deposition over the last 4 m.y. produced largely vertical and relatively cylindrical diapirs. This dynamic may have facilitated very effective vertical hydrodynamic communication in the region both along radial fault systems directly caused

by salt growth and secondary faulting between domes in response to local sediment diversion by them.

A high level of vertical hydrodynamic communication in the section is also evidenced by the large number of oil and gas fields with stacked accumulations. For fields in this region as a whole, on average, a gross vertical section of 5705 ft (1738 m) is saturated with hydrocarbons and the greatest thickness between the shallowest and deepest reservoirs at a single field is 16,644 ft (5073 m) (Earth Science Associates, 2012).

The modest SAR maximum would have minimized syndepositional compaction disequilibrium and the subsequent 4 m.y. of relatively low and stable sedimentation may have provided sufficient opportunities for overpressured compartments to equilibrate. Equilibration would have been enhanced by vertical hydrodynamic communication provided by the steady formation and reactivation of vertically extensive, high-dip faults formed by salt movement and sedimentation during and subsequent to the regional SAR maximum.

Louisiana Outer Shelf

The Louisiana Outer Shelf has a dramatically higher pressure regime than the Louisiana Inner Shelf. The Louisiana Outer Shelf is centered on the modern shelf-slope break (here taken to be the 500 ft (152 m) isobath), extending approximately 30 mi (48.28 km) to the north and south of it (Figure 9A). The average of the depths to the top of hard geopressure is 9350 ftbml (2850 mbml), which is 4723 ft (1440 m) or one-third shallower than in the Louisiana Inner Shelf region. The shallowest depth at which hard geopressure is encountered is in the 4500-5500 ft (1372-1676 m) interval, 2000 ft (609.6 m) shallower than to the north. The much higher pressure gradients and mud weights in the Louisiana Outer Shelf versus the Inner Shelf regions were seen at all depth intervals.

Figure 9. The depth to the first occurrence of hard geopressure (0.7 psi/ft [15.83 kPa/m]). (A) shows the depth of hard geopressure in plan view, the boundaries of the four regions identified in the study, and the location of the cross section (C). Figure (B) shows the same surface in 3-D with a vertical exaggeration factor of 10 and follows the same legend as in (A). The surface has been smoothed for better visibility in 3-D, and the location of the cross section (C) is shown by a vertical wall. Figure (C) (also shown in Figure 1C) has a black line superimposed following the top of hard geopressure. The three intersecting regions identified in (A) are shown; the inverted black triangle shows the location of the coast.

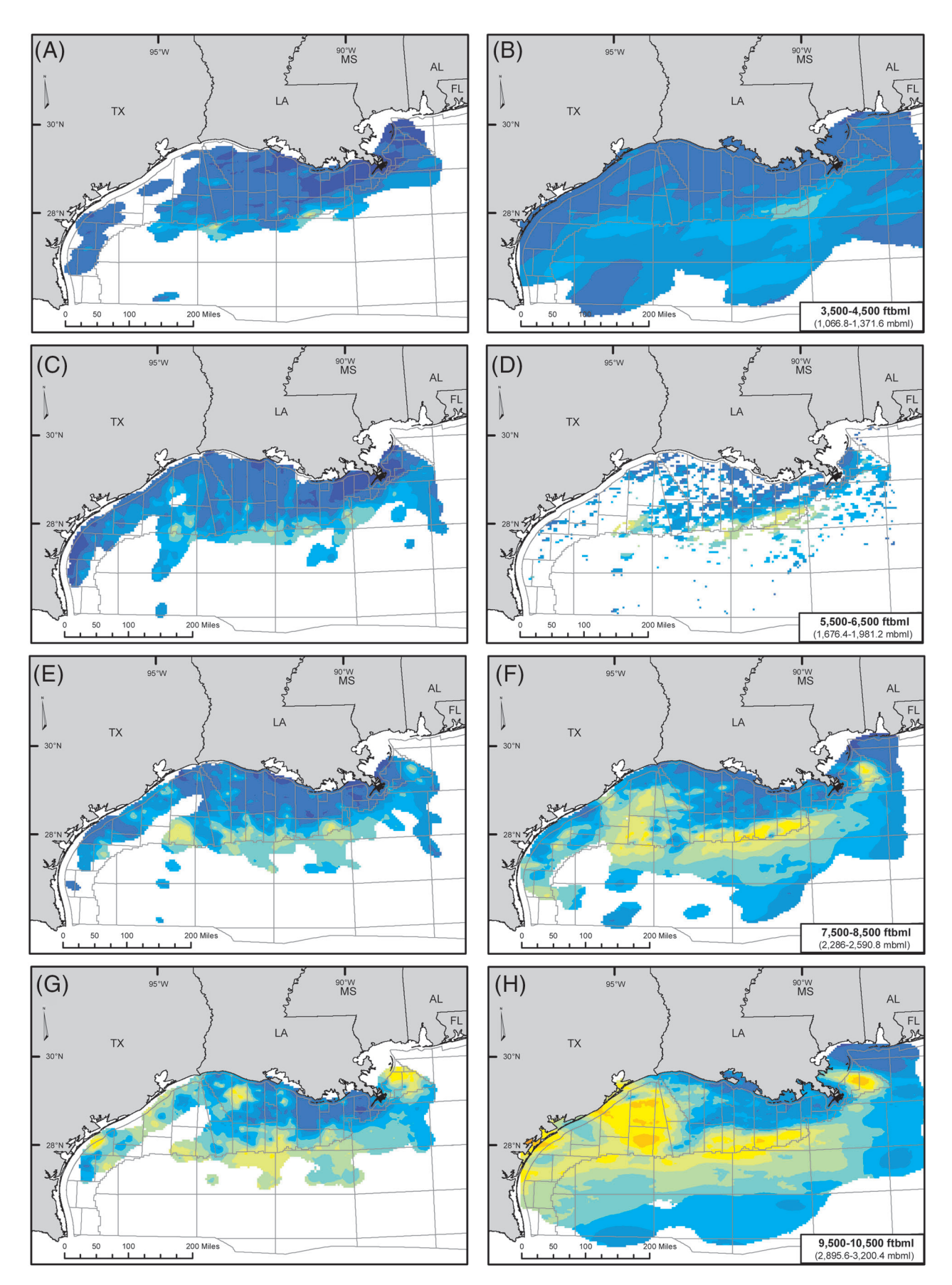


Figure 10. Maps of estimated pressure gradient (left column) and mud weight (right column) by depth interval.

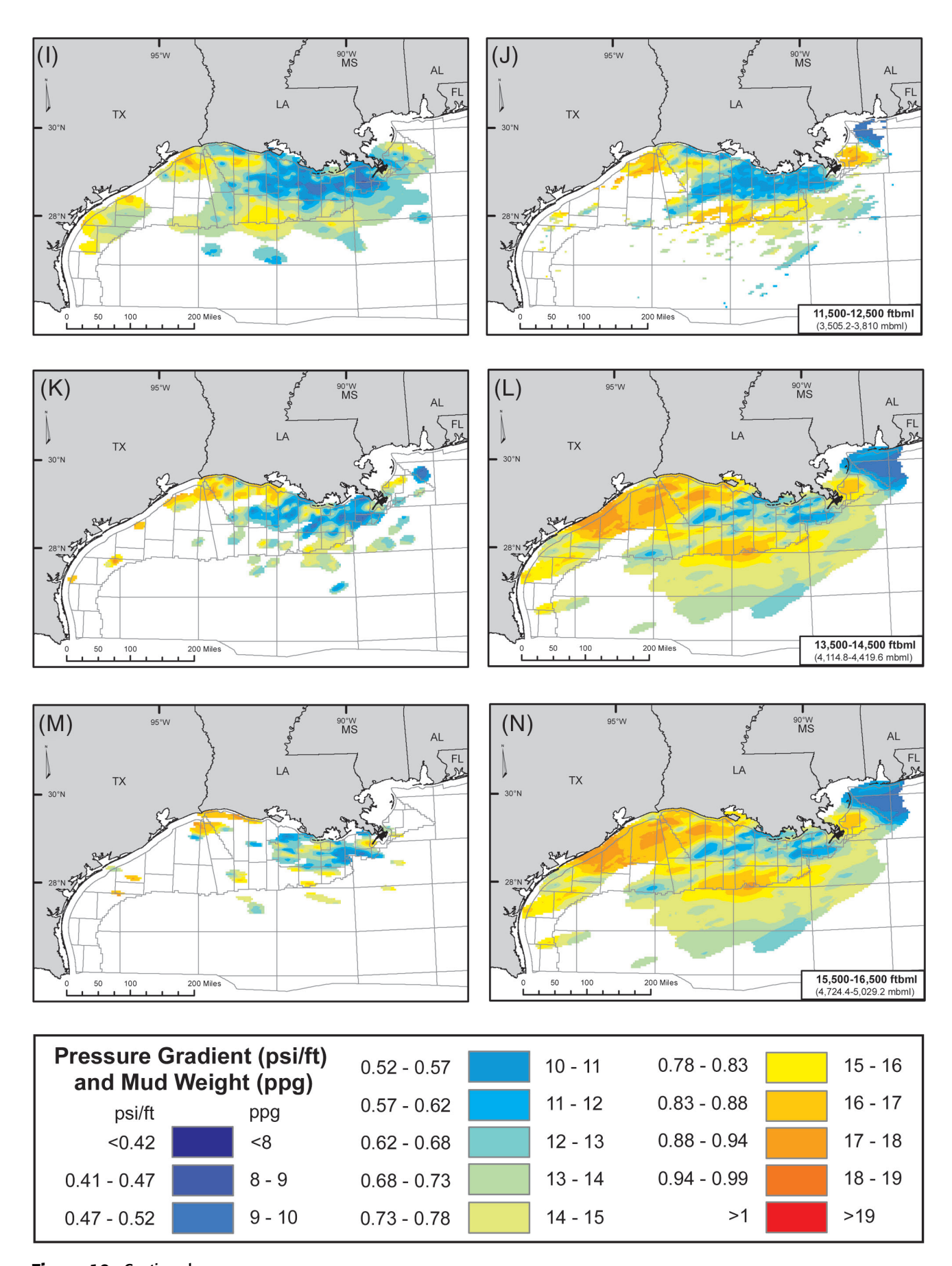


Figure 10. Continued.

The Louisiana Outer Shelf region is coincident with major Pliocene-Pleistocene depocenters (Snedden et al., 2013). Until the early Pliocene, deposition rarely exceeded 1000 ft/m.y. (305 m/m.y.). Then, a major progradation pushed the shelf margin to the northern border of Louisiana Outer Shelf region and SAR in the north part of the region exceeded 3000 ft/m.y. (914.4 m/m.y.) for the first time. Between then and the Calabrian Age of the Pleistocene Epoch, although the shelf edge prograded only a maximum of another 30 mi (48 km) south, the largest sediment loads shifted several times laterally between the Red, Mississippi, and Tennessee Rivers distributaries. This led to very focused pods of very high-SAR deposition (from 6000 to over 10,000 ft/m.y. (1828.8-3048 m/m.y.) and low-SAR (<1000 ft/m.y. [305 m/m.y.] bypassed areas between them. Then, from the Calabrian Age (1.3 Ma) through the end of the Pleistocene Epoch, most of the region was subjected to SARs in the 6000-9000 ft/m.y. (1829–2743 m/m.y.) range.

The initiation of major salt growth, compared to the region immediately to the north, was postponed to early Pliocene and has remained active, if episodic, since. In the Louisiana Outer Shelf region, the morphology of salt intrusions into the overlying section became less cylindrical. In the southern part of the regime (coincident with the modern shelf edge) basinward sediment transport formed extensive salt canopies (Hall, 2002).

The large increase in the pore pressure in the Louisiana Outer Shelf region correlates with a sedimentation that, starting in the early Pliocene, was very high and localized, followed by a major late Pleistocene blanketing, region-wide high-SAR event. This sequence of events could have contributed to greater compaction disequilibrium. Lateral pressure release, along strata, could have been retarded in an environment in which dip changes over short distances and by high magnitudes. Vertical pressure release in a rapidly accumulating sand—shale section is impeded by differentially higher compaction of shales with concomitant loss of vertical permeability.

While growth of salt structures would have provided the same types of avenues for vertical communication as to the north, these apparently were insufficient to offset the rate at which pressure grew

due to the extreme accumulation of overburden. As evidence of the weaker vertical hydrodynamic communication in the Louisiana Outer Shelf region, the average gross thickness of hydrocarbon saturation at discovered fields is 4121 ft (1256 m), 27% thinner than the gross saturated section at fields in the Inner Louisiana Shelf.

Deep Water

Deep Water south of Louisiana, starting in the upper modern slope and (presumably) extending to the Sigsbee Escarpment, marks a reversal of regional pressure regime relative to the Louisiana Outer Shelf region to the north. This region shares the very high post-early Pliocene average SARs of its northern neighbor and experienced local SARs that were even higher. However, compared to the section to the north, this region is almost completely covered by salt canopies, interrupted locally by minibasins.

Although the Deep Water region received post-Early Pliocene sedimentation at no less than the rate in the Louisiana Outer Shelf, the miniature dimensions of Deep Water minibasins may explain the more efficient equilibration of compaction within them. Geometrically at all depths, more of the total pore volume of a minibasin is closer to the salt-flanks of the basin and therefore also closer to fault systems associated with them than in a larger salt-bounded rock volume. Oil and gas found on minibasin flanks evidence active fluid migration from minibasin centers, which would provide fairways to reduce pressure as well as shuttle hydrocarbons. Although it cannot be systematically studied without regional maps on the top and bottom of salt, the intrusion of large volumes of lower mass rock may also play a role in occasionally lowering the average pressure gradient in this region (compared to those in the Louisiana Outer Shelf). Irrespective of local and regional causes, in the Louisiana Deep Water region, empirically, the entire pressure field shifts to a lower pressure regime starting about 30 mi (48 km) south of the modern shelf margin.

Texas Shelf and Slope

The pressure regimes to the east and south of the Texas coast are unified by their heterogeneity (Figure 9A and B). Compared to the region south of Louisiana, there were large-scale differences in the course of sedimentation, and there was a smaller volume of original salt. Heterogeneity was also added because over the last 3 m.y., the western-most part of the depositional systems concentrated south of Louisiana strayed into the eastern part of the Texas shelf and slope region.

The geologic development of the GOM south of the Louisiana coast since middle Miocene time was dominated by massively high-rate sedimentation from the north from a set of river distributaries that, from the perspective of the receiving basin, could be considered a laterally extensive but single source. The highest rates of sedimentation frequently switched between distributaries extending from the Red River in the west through the Mississippi River channels to the Tennessee River in the east; the sedimentary front also moved north and south across the modern shelf.

However, on the Texas coast, the principal fluvial axes (after the Oligocene Epoch) were more laterally stable and delivered sediment to the basin at a much lower rate. Therefore, in relative terms, sedimentation was subject to greater redistribution by longshore currents than south of Louisiana. High SAR areas perpendicular to the modern coast are coincident with the successive fluvial systems (e.g., along the courses of the modern Rio Grande in the south and the modern Brazos, Trinity, and Sabine Rivers in the north) and exhibit higher pressures than the intervening areas between them. The latter was much more commonly a barrier-strand plain environment over the entire Neogene, and therefore, subject to lower SARs; over most depth intervals, it is a lower pressure environment.

In the eastern Texas region, particularly from the late Pliocene until the beginning of the late Pleistocene, the greater Mississippi river systems that provided so much sediment so quickly south of Louisiana also migrated west. During this period, in the High Island (abbreviated as HI and HIA in Figure 1A) and West Cameron (WC) protraction areas and in the northeastern portion of East Breaks (EB), local SARs exceeded 5000 ft/m.y. (1524 m/m.y.).

Because of the lack of drilling and discoveries in this area below the base of the Pliocene, it is unknown if the high pressure of the Pliocene–Pleistocene extends to the distal Miocene section below.

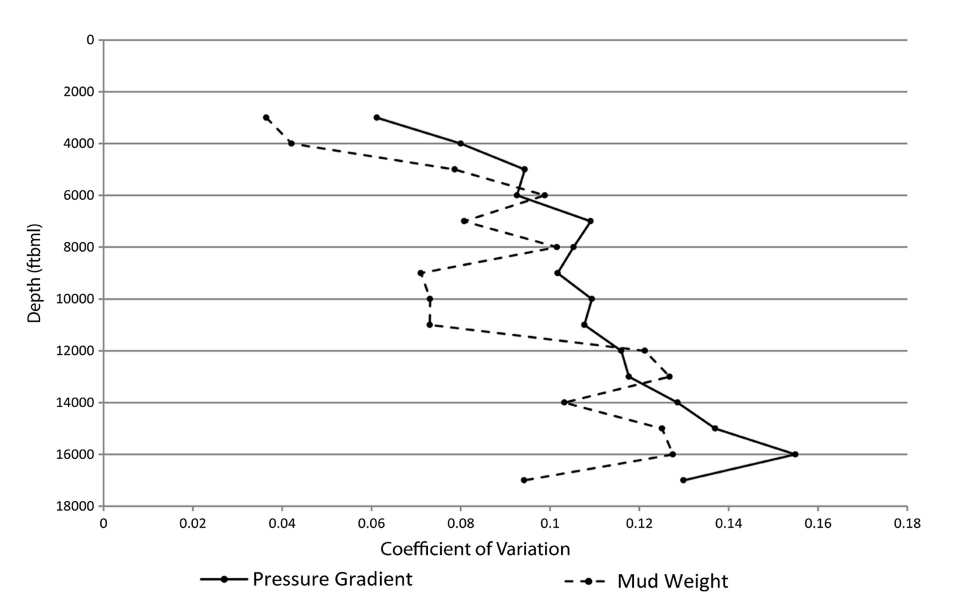
The heterogeneity of the pressure field in the Texas region can also be seen in the hot spot map in Figure 8B. Although only the differences in mud weight between the 9500–10,500 ftbml (2896–3200 mbml) and 10,500–11,500 ftbml (3200–3505 mbml) are shown, most of the clusters of highly anomalous changes in pressure are in the Texas region, and these hot spots cover a very large percentage of the area; both positive and negative anomalies are evident.

Vertical Transition Zones

Changes in the pressure gradient and mud weight in depth highlight two important regularities. First, the increase of the reservoir initial pressure gradient is a much more consistent function of depth than is mud weight. Mud weight maintained by drillers is a function of the pressure in the bottom of the well, but it is also a reflection of the driller's strategy for mitigation of the operational risks associated with high pore pressure. Therefore, the decision to weight-up the drilling fluid and to drill overbalanced may be taken at a depth shallower than the anticipated increase in pressure is expected to occur. As different operators may have varying strategies, the variation in mud weights exceeds the variation in the underlying pressure field.

This relationship is seen clearly in Figure 11 where sharp excursions in the coefficient of variation for mud weights occur in the 4500-8500 ftbml (1372-2591 mbml) range and again at the 11,500-12,500 ftbml (3505-3810 mbml) interval. It is also obvious in Figure 10D, where the error clipping of the mud weight map for the 5500-6500 ftbml (1676-1981 mbml) interval leaves only a small percentage of the original map with high enough spatial continuity to be included. In the intervals immediately below and above the 5500-6500 ftbml (1676-1981 mbml) interval (which are not shown), the impact of low spatial continuity on the percent of the map retained after clipping is even more pronounced. Only 6% of the original area of the 4500-5500 ftbml (1372-1676 mbml) interval was retained after clipping, and only 2% of the 6500-7500 ftbml (1981-2286 mbml) interval passed the minimum

Figure 11. The coefficient of variation (the average of every cell's kriging standard error divided by the associated prediction in the clipped map) for the fifteen 1000 ft (305 m) depth intervals studied. The coefficient of variation for initial reservoir pressure gradient increases relatively smoothly as a function of depth. In contrast, the coefficient of variation for mud weight moves sharply at the 5000 ft (1524 m) interval, reverses at the 8000 ft (2438 m) interval and increases sharply again at the 12,000 ft (3658 m) depth.



certainty threshold. Finally, these depths were also the ones in which the estimated anisotropy of the pressure field, as measured by the mud weight and initial reservoir pressure gradient were least similar (Tables 3 and 4, Appendix 2).

The second important Gulf of Mexico-wide finding on the pressure field in the vertical dimension occurs in the range 11,500-13,500 ftbml (3505-4115 mbml) range. This is evidenced in the mud weight data by a 72% increase in KSE between the shallower and deeper halves of that range (Table 6, Appendix 2). In the initial reservoir pressure gradient data, the spatial continuity in the shallower half of this zone is normal but decreases significantly in the deeper half. While both variables return to normal patterns of spatial continuity in the 13,500-14,500 ftbml (4114-4420 mbml) interval, it begins to decline again going deeper. In the deeper case, this more likely reflects a decreasing number of observations rather than an underlying change in the nature of the pressure field.

Analytic Limitations

It is important to understand that because this study is regional, there is scale limitation in analyzing local causes of abnormal pressures. Two important sources of local variation in pressure are below the spatial resolution of an analysis where the cell size used was 9 mi² (23 km²). First, the influence of hydrocarbon column height on local pressure is averaged out,

because in the GOM, the average hydrocarbon-saturated area of reservoirs is only slightly over 1000 acres (4 km²), 17% of the cell size. Second, while some seals are regional, the seals for hydrocarbon accumulations are necessarily the same area as the area of saturation, hence, almost always smaller than the cell size used here.

A related constraint was accessible data. Maps of the top and bottom of salt, facies/grain-size maps (or digital log files from which they could be constructed), and local structure maps at the locations of pressure observations are not publically available. Therefore, use of these important geologic characteristics as explanatory variables for pressure variation was impossible. In this analysis, only the spatial distribution of the 56,252 observations on reservoir pressure and mud weight could be brought directly into the analysis and used in the predictions made. Hydrocarbon column height, the influence of seals (and faults through them), salt, and local structure are all included in this analysis collectively, but their individual effects cannot be separately identified.

CONCLUSIONS

The pressure field across connected rock pores is fundamental to determining the distribution of fluids, gases, and their solutes in the subsurface; it strongly influences the sizes and locations of oil and gas accumulations. Of even more urgent significance,

112

subsurface pressure, particularly when it changes suddenly or unexpectedly, can have catastrophic impacts on the safety of drilling wells (Wassel, 2012). Our methodological contributions to pressure analysis arise from applying geostatistical techniques to very large databases of pressure-related observations. This not only provided estimates of the pressure field but, critically, a consistent basis for evaluating the confidence those estimates should enjoy in geologic and engineering practice. Applying this approach to the GOM allowed us to define broad, lateral and vertical variations in pressure related to regional geologic controls. These findings are reflected not only in pressure gradient and mud weight maps by depth but also in derivative mapping of rates of change in pressure (in all three dimensions) and in investigation of the spatial continuity of the pore pressure field throughout the sedimentary section of the basin.

Assessing and communicating the empirical confidence in the analysis was a central goal of the study. Ordinary kriging provided two immediate advantages in support of that goal. First was to evaluate local confidence intervals surrounding estimated pressure for each 9 mi 2 × 1000 ft (23.3 × 305 m) grid cell mapped. As in classical statistics, this supports making empirically founded and consistent decisions on usefulness of the values estimated in the study.

Second, we exploited the estimation variance produced by kriging to geographically clip the maps based on a uniform information criteria. Although we used more than 55,000 observations over a rock volume of roughly 422,000 mi³ (1.76 million km³), only about 27% of that volume met the cutoff criteria by adding significantly more information than simply computing Gulf of Mexico-wide statistics that ignore the spatial (hence geologic) dimensions of the data. All gridding algorithms produce estimates of variable values at any distance from control and create authoritative-looking maps based on them. Here, we have contributed a method for setting a consistent boundary beyond which such a map should not be believed.

The probabilistic approach purposefully allows users to change the probability limits of confidence intervals, or the cutoff threshold for map extents, in light of the purpose to which maps are put and to directly integrate setting those parameters with

decisions that account for the cost of error in accepting analytic results.

The study defined four regional pressure regimes within the GOM that highlight the central role of the timing and magnitude of sedimentation on the pressure field, a relationship made much more complex by mobile salt. Broad compartments were reflected in both the initial reservoir pressure and mud weight data and in analyzing the variance in over 50,000 observations.

Although the use of both initial reservoir pressures and drilling mud weight drew generally similar regional pictures, the study also showed how mud weight data can conflate natural changes in the pressure regime with engineering strategies. This points to the importance of using multiple indicators that signal changes in the pressure regime.

The regional approach misses the fine detail of high-density geophysical information and site-specific burial history/fluid flow modeling. It also glosses local biases in the data (such as wells being preferentially drilled on structural highs). However, it does provide a strong foundation for further regional hydrodynamic analysis based in part on the existing spatial distribution of pressure. This is an important complement to hydrocarbon analysis of migration pathways and the formation of regional pressure compartments, within which hydrodynamic systems are functionally closed. An empirically based regional perspective also forms a solid, independent foundation for site-specific pressure prediction ahead of drilling.

APPENDIX 1

There are at least two perspectives for analysis of the regional distribution of pore pressures in an offshore setting. First is to focus on the actual existing pressure at a depth. A pressure gradient (e.g., psi/ft) in which the observed pressure at a specific vertical depth relative to an absolute datum, like mean sea level (MSL), is divided by that vertical depth will recover the original pressure through multiplying the gradient by the vertical depth. Mud weight is a linear transformation of the same relationship: mud weight in pounds per gallon (ppg) multiplied by 0.05187 times the vertical depth also recovers the pressure at depth.

When the setting is offshore, the actual pressure at any depth below the seafloor is a weighted sum. The first component is the pressure generated by the water column (expressed as a gradient, here 0.465 psi/ft, [10.52 kPa/m]) times the decimal fraction of

total depth comprised by the water column. The second component is the force generated between the seafloor and the target depth. This too can be expressed as a gradient (e.g., in psi/ft, where the depth is relative to the sea floor) and is multiplied by the decimal fraction of the total depth (from MSL) that extends from the seafloor to the target depth. Summing both weighted components yields an average pressure gradient between the (MSL) datum and total target depth. This average gradient, when multiplied by total depth (below MSL), also recovers the pressure at the target depth.

The objective of this approach is to model the actual pressure that would be encountered at a specific vertical depth, addressing the needs of operational safety. It also provides the foundation for understanding the influence of pressures that motivate fluid/gas migration and affect seal competence. This approach was adopted in this paper. All pressure gradients (and mud weights) are expressed relative to MSL and represent averages that include both the pressure generated in the water column and the sedimentary column below it.

The second approach segregates the force generated in the water column and the force generated from the sea floor to the target depth. The former portion is then subtracted, leaving only the pressure generated in the rock column. Removing the influence of the water column reveals a valuable geomechanical perspective on how pressure changes between the top of the sedimentary section and any specific depth below it. However, the pressure calculated this way does not exist in nature; it is a derivative variable that postulates what pressure at depth would be if the force generated by water column was removed.

While adopting the first approach of including the influence of the water column on pressure at depth, in making the maps in this paper, we defined the depth slices relative to the sea floor. There were two reasons for this decision: (1) it is a common practice in industry to create depth slices relative to the sea floor, and (2) if the depth slices had been taken relative to MSL, the shallow depth slices would have terminated in the water column

in the parts of the GOM with water depths greater than 2500 ft (762 m).

The approach of predicting the actual pressure gradient and mud weight at depth, as opposed to theoretical variables that would be obtained by removing the water and the decision to map depth slices relative to the sea floor are independent of each other. The underlying data (plus bathymetric data) supports the no-water-column approach, and the depth slices could be recalculated from any other relative datum (like the sea floor or, for instance, the top of Pliocene) or from a different absolute datum.

However, maps made under these two approaches are different. On the shelf, where the water is a very small fraction of the total depth to a target, removing the influence of the water would have a minimal effect. For instance, in Figure 9A, the average depth to the 0.7 psi/ft (15.8 kPa/m) gradient in the Louisiana Inner Shelf region is 14,049 ftbml (4282 mbml) when calculated including the force of the water column; it would be 14,139 ftbml (4310 mbml) if the water column was removed, 0.6% deeper. Beyond the shelf–slope break, the water column is a larger share of total depth. The average depth to the 0.7 psi/ft (15.8 kPa/m) gradient in the deep water region is 13,344 ftbml (4067 mbml) when the force exerted by the water column is included; if it is removed, the average would be 15,515 ftbml (4729 mbml), 16% deeper.

Not surprisingly, removing the force of the water column reduces the total pressure at any depth below the mud line, and that reduction is proportional to the fraction that water depth comprises of total depth. Inclusion or exclusion of the influence of water does not change the conclusions of this analysis, although it would change the details of the maps. By including water depth, the maps presented here reflect actual pressures at depth rather a derivative variable, which while useful is not the focus of this study.

APPENDIX 2

Table 1. Summary of Pressure Gradient Data (psi/ft)

Depth Interval (ftbml)	N	Minimum	Maximum	Mean	Standard Deviation	Median
2500-3500	565	0.44	0.68	0.49	0.04	0.47
3500-4500	888	0.43	0.82	0.50	0.05	0.47
4500-5500	1058	0.43	0.79	0.51	0.06	0.47
5500-6500	1329	0.43	0.80	0.52	0.07	0.48
6500-7500	1521	0.43	0.87	0.52	0.08	0.49
7500-8500	1437	0.43	0.93	0.54	0.09	0.50
8500-9500	1377	0.43	0.88	0.55	0.10	0.51
9500-10,500	1217	0.45	0.90	0.58	0.11	0.55
10,500-11,500	1017	0.43	0.92	0.61	0.12	0.57
11,500-12,500	861	0.43	0.96	0.63	0.12	0.60
12,500-13,500	606	0.46	0.94	0.65	0.13	0.64
13,500-14,500	460	0.46	1.00	0.67	0.14	0.67
14,500-15,500	352	0.46	1.00	0.70	0.14	0.70
15,500-16,500	182	0.47	0.96	0.70	0.13	0.70
16,500-17,500	106	0.47	0.96	0.75	0.13	0.78

Table 2. Summary of Mud Weight Data (ppg)

Depth Interval (ftbml)	Ν	Min	Max	Mean	Standard Deviation	Median
2500–3500	2263	8.0	17.3	10.1	1.1	9.8
3500-4500	3070	8.0	16.2	10.2	1.2	9.9
4500-5500	2897	8.0	16.8	10.7	1.5	10.5
5500-6500	2951	8.3	18.8	11.2	1.7	10.8
6500-7500	3438	8.1	17.2	11.4	1.9	11.0
7500-8500	3889	8.2	19.0	11.6	2.1	11.3
8500-9500	3916	8.0	19.6	11.9	2.3	11.6
9500-10,500	4143	8.0	18.4	12.3	2.5	12.0
10,500-11,500	3704	8.0	18.8	12.7	2.6	12.5
11,500-12,500	3535	8.0	19.4	13.2	2.7	13.2
12,500-13,500	2954	8.0	19.6	13.8	2.7	14.2
13,500-14,500	2319	8.0	19.0	14.2	2.6	14.4
14,500-15,500	1915	8.0	19.9	14.1	2.8	14.6
15,500-16,500	1351	8.0	19.7	14.7	2.6	15.2
16,500-17,500	931	8.0	19.4	15.2	2.6	15.8

Table 3. Semivariogram Analysis of Pressure Gradient Data

Depth Interval (ftbml)	Obs	Lag Size (ft)	Ellipse Eccentricity	Anisotropy (deg.)	Nugget (psi/ft) ²	Shape (Θ_e)	Range (Θ_r) (ft)	Partial Sill (Θ_s) $(psi/ft)^2$
2500–3500	565	80,144	2.18	47	1.23×10^{-4}	0.56	961,724	1.71×10^{-03}
3500-4500	888	32,159	2.77	78	2.70×10^{-04}	0.89	385,910	2.34×10^{-03}
4500-5500	1,058	54,669	1.89	17	0	0.54	656,034	3.46×10^{-03}
5500-6500	1,329	78,120	1.15	32	7.58×10^{-06}	0.58	476,989	4.59×10^{-03}
6500-7500	1,521	82,014	1.34	145	1.02×10^{-04}	0.51	984,188	6.14×10^{-03}
7500-8500	1,437	42,651	1.56	114	2.35×10^{-04}	0.54	511,811	6.85×10^{-03}
8500-9500	1,377	22,966	1.73	102	3.68×10^{-04}	0.70	275,591	6.32×10^{-03}
9500-10,500	1,216	19,685	1.20	98	6.68×10^{-04}	0.68	236,220	7.10×10^{-03}
10,500-11,500	1,015	9843	1.21	163	2.46×10^{-03}	0.98	118,110	6.99×10^{-03}
11,500-12,500	861	29,528	1.81	96	1.76×10^{-04}	0.73	354,331	1.10×10^{-02}
12,500-13,500	605	9350	2.83	110	1.18×10^{-03}	1.63	88,254	1.04×10^{-02}
13,500-14,500	460	10,719	1.61	68	9.55×10^{-04}	1.16	128,640	1.33×10^{-02}
14,500-15,500	352	29,390	2.98	91	1.53×10^{-03}	1.08	200,318	1.37×10^{-02}
15,500-16,500	182	36,089	2.99	97	5.82×10^{-04}	0.99	178,413	1.51×10^{-02}
16,500-17,500	106	21,050	2.98	109	1.67×10^{-03}	1.52	111,696	1.54×10^{-02}

Table 4. Semivariogram Analysis of Mud Weight Data

Depth Interval (ftbml)	Obs	Lag Size (ft)	Ellipse Eccentricity	Anisotropy (deg.)	Nugget (ppg²)	Shape (Θ_e)	Range (Θ_r) (ft)	Partial Sill (Θ_s) (ppg^2)
2500-3500	2059	18,044	2.04	81	0.61	2.00	216,535	0.25
3500-4500	2722	34,367.	2.65	69	0.64	2.00	412,418	0.49
4500-5500	2413	8202	1.37	104	0.65	1.12	46,581	0.84
5500-6500	2366	11,483	1.91	75	0.59	0.58	137,795	1.61

(continued)

Table 4. Continued

Depth Interval (ftbml)	Obs	Lag Size (ft)	Ellipse Eccentricity	Anisotropy (deg.)	Nugget (ppg ²)	Shape (Θ_e)	Range (Θ_r) (ft)	Partial Sill (Θ_s) (ppg^2)
6500-7500	2652	4921	1.00	75	0.72	2.00	34,485	1.45
7500-8500	2890	29,610	1.88	83	1.01	0.91	355,312	2.88
8500-9500	2985	36,020	2.61	87	2.56	1.90	432,228	2.18
9500-10,500	3003	43,842	2.78	89	2.54	2.00	526,093	2.80
10,500-11,500	2680	39,587	2.09	88	2.73	2.00	475,023	3.16
11,500-12,500	2504	13,123	2.98	71	1.47	0.53	157,480	3.06
12,500-13,500	2040	16,404	2.80	64	1.67	0.69	196,850	3.68
13,500-14,500	1633	40,876	2.99	73	1.86	0.92	490,531	3.66
14,500-15,500	1275	26,932	2.48	91	1.04	0.66	323,199	4.54
15,500-16,500	889	17,516	2.33	70	1.33	0.81	210,213	4.57
16,500-17,500	587	13,727	2.79	78	1.65	1.95	164,711	3.88

Table 5. Characteristics of (Clipped) Grids from Ordinary Kriging Estimation of Reservoir Pressure Gradient Data by 1000 ftbml Intervals

		For Depth	Interval		For Entire Map			
Depth Interval (ftbml)	Ave. Mean (psi/ft)	Min. Mean (psi/ft)	Max. Mean (psi/ft)	Ave. KSE (psi/ft)	Percent of Map Remaining after Clip	Cross-Validation RMSE		
2500-3500	0.49	0.45	0.63	0.03	29	0.03		
3500-4500	0.50	0.44	0.77	0.04	23	0.03		
4500-5500	0.53	0.44	0.78	0.05	35	0.03		
5500-6500	0.54	0.44	0.74	0.05	27	0.03		
6500-7500	0.55	0.44	0.78	0.06	31	0.04		
7500-8500	0.57	0.45	0.78	0.06	26	0.05		
8500-9500	0.59	0.46	0.81	0.06	26	0.06		
9500-10,500	0.64	0.47	0.85	0.07	27	0.06		
10,500-11,500	0.65	0.47	0.87	0.07	18	0.06		
11,500-12,500	0.69	0.47	0.93	0.08	25	0.06		
12,500-13,500	0.68	0.46	0.92	0.08	9	0.08		
13,500-14,500	0.70	0.47	0.95	0.09	12	0.07		
14,500-15,500	0.73	0.47	0.97	0.10	10	0.06		
15,500-16,500	0.71	0.48	0.92	0.11	6	0.08		
16,500-17,500	0.77	0.49	0.96	0.10	3	0.09		

Table 6. Results of Ordinary Kriging Estimation of 1000 ft Interval for Mud Weight

Depth Interval (ftbml)		For Depth	n Interval	For Entire Map		
	Ave. Mean (ppg)	Min. Mean (ppg)	Max. Mean (ppg)	Ave. KSE (ppg)	Percent of Map Remaining after Clip	Cross-Validation RMSE
2500-3500	10.15	8.85	12.43	0.37	49	0.88
3500-4500	10.21	8.59	12.93	0.43	62	0.85
4500-5500	10.68	8.62	14.98	0.84	6	0.95
						(aamtimus d

Table 6. Continued

Depth Interval (ftbml)		For Depth	ı Interval		For Entire Map			
	Ave. Mean (ppg)	Min. Mean (ppg)	Max. Mean (ppg)	Ave. KSE (ppg)	Percent of Map Remaining after Clip	Cross-Validation RMSE		
5500-6500	11.13	8.80	15.18	1.10	11	1.03		
6500-7500	11.39	8.80	15.73	0.92	2	1.16		
7500-8500	11.82	8.43	16.17	1.20	44	1.19		
8500-9500	12.10	8.82	16.01	0.86	56	1.57		
9500-10,500	12.58	8.91	17.60	0.92	64	1.61		
10,500-11,500	13.00	8.79	18.43	0.95	60	1.68		
11,500-12,500	13.53	9.32	17.37	1.64	17	1.57		
12,500-13,500	14.04	9.06	17.83	1.78	29	1.65		
13,500-14,500	14.34	9.18	17.83	1.48	39	1.57		
14,500-15,500	14.47	9.04	17.97	1.81	21	1.58		
15,500-16,500	14.90	9.11	18.19	1.90	20	1.77		
16,500-17,500	15.82	10.16	18.73	1.49	17	1.40		

REFERENCES CITED

- Anselin, L., 1995, Local indicators of spatial association–LISA: Geographical Analysis, v. 27, no. 2, p. 93–115.
- Bethke, C. M., 1985, A numerical model of compaction-driven groundwater flow and heat transfer and its application to paleohydrology of intracratonic sedimentary basins: Journal of Geophysical Research, v. 90, p. 6817–6828, doi:10.1029/JB090iB08p06817.
- BOEM (Bureau of Ocean Energy Management Regulation and Enforcement), 2011, Estimated oil and gas reserves—Gulf of Mexico OCS Region: OCS Report BOEMRE 2011-045, p. 1.
- BSEE (Bureau of Safety and Environmental Enforcement), 2012: accessed November 27, 2012, http://www.data.bsee.gov/homepg/data_center/other/pios/pmaster.asp.
- Burke, L. A., S. A. Kinney, R. F. Dubiel, and J. K. Pitman, 2012, Regional map of the 0.70 psi/ft pressure gradient and development of the regional geopressure-gradient model for the onshore and offshore Gulf of Mexico basin, U.S.A.: GCAGS Journal, v. 1, p. 97–106.
- Carcione, J. M., and H. B. Helle, 2002, Rock physics of geopressure and prediction of abnormal pore fluid pressures using seismic data: CSEG Recorder, v. 27, p. 8–32.
- Dickenson, G., 1953, Geological aspects of abnormal reservoir pressures in Gulf Coast Louisiana: AAPG Bulletin, v. 37, no. 2, p. 410–432.
- Dvorkin, J., G. Mavko, and A. Nur, 1999, Overpressure detection from compressional- and shear-wave data: Geophysical Research Journal, v. 26, p. 3417–3420.
- Earth Science Associates, 2012, GOM³ 6.0: Long Beach, Earth Science Associates.
- Galloway, W. E., P. E. Ganey-Curry, X. Li, and R. Buffler, 2000, Cenozoic depositional history of the Gulf of Mexico basin: AAPG Bulletin, v. 84, no. 11, p. 1743–1774.

- Galloway, W. E., T. L. Whiteaker, and P. E. Ganey-Curry, 2009, History of Cenozoic North American drainage basin evolution, sediment yield, and accumulation in the Gulf of Mexico basin: Geosphere, v. 7, no. 4, p. 938–973.
- Hall, S. H., 2002, The role of autochthonous salt inflation and deflation in the northern Gulf of Mexico: Marine and Petroleum Geology, v. 19, no. 6, p. 649–682, doi:10.1016/S0264-8172(02)00025-9.
- Henning, A., Y. Najwa, M. A. Addis, and A. Warrington, 2002, Pore-pressure estimation in an active thrust region and its impact on exploration and drilling, *in* A. R. Huffman and G. Bowers, eds., Pressure regimes in sedimentary basins and their prediction: AAPG Memoir 76, p. 89–105.
- Huffman, A. R., 2002, The future of pressure prediction using geophysical methods, *in* A. R. Huffman and G. Bowers, eds., Pressure regimes in sedimentary basins and their prediction: AAPG Memoir 76, p. 217–233.
- Isaaks, E. H., and R. M. Srivastava, 1989, An introduction to applied geostatistics: New York, Oxford University Press, 561 p.
- Johnston, K., J. M. Ver Hoef, K. Krivoruchko, and N. Lucas, 2001, ArcGIS 9 Using Geostatistical Analyst: Redlands, CA, Environmental Systems Research Institute, 300 p.
- Law, B. E., and C. W. Spencer, 1998, Abnormal pressure in hydrocarbon environments, *in* B. E. Law, G. F. Ulmishek, and V. I. Slavin, eds., Abnormal pressures in hydrocarbon environments: AAPG Memoir 70, p. 1–12.
- Lesso, W. G., Jr., and T. M. Burgess, 1986, Pore pressure and porosity from MWD measurements: Society of Petroleum Engineers/International Association of Drilling Contractors Drilling Conference, SPE-14801-MS, 14 p.
- Louie, J. N., and A. M. Asad, 1994, Seismic amplitude versus offset (AVO) character of geopressured transition zones, *in* P. J. Ortoleva ed., Basin Compartments and Seals: Tulsa, OK, AAPG Memoir 61, p. 131–139.

- Minerals Management Service, Gulf of Mexico OCS Region, 2001, 2000 Assessment of conventionally recoverable hydrocarbon resources of the Gulf of Mexico and Atlantic outer continental shelf as of January 1, 1999 (CD-ROM): New Orleans, Louisiana, 631 p.
- Muffler, L. J. P., ed., 1979, Assessment of geothermal resources of the United States—1978: Geological Survey Circular 790, 170 p.
- Peel, E. J., C. J. Travis, and J. R. Hossack, 1995, Genetic structural provinces and salt tectonics of the Cenozoic offshore U.S. Gulf of Mexico: A preliminary Analysis, *in* M. P. A. Jackson, D. G. Roberts, and S. Snelson eds., Salt tectonics: a global perspective: AAPG Memoir 65, p. 153–175.
- Sayers, C. M., G. M. Johnson, and G. Denyer, 2002, Predrill pore pressure prediction using seismic data: Geophysics, v. 67, no. 4, p. 1286–1292, doi:10.1190/1.1500391.
- Sharp, J. M., Jr., 1976, Momentum and energy balance equations for compacting sediments: Mathematical Geology, v. 8, no. 3, p. 305–322, doi:10.1007/BF01029275.

- Snedden, J., W. E. Galloway, P. E. Ganey-Curry, and T. Whiteaker, 2013, Gulf basin depositional synthesis project (phase VII): University of Texas, Austin, Institute of Geophysics.
- Throndsen, T., and M. Wangen, 1998, A comparison between 1-D, 2-D and 3-D basin simulations of compaction, water flow and temperature evolution, *in* S. J. Düppenbecker and J. E. Iliffe, eds., Basin modeling: Practice and progress: London, Geological Society of London, Special Publications 141, p. 109–116.
- Wallace, R. H., Jr., T. F. Kraemer, R. E. Taylor, and J. B. Wesselman, 1979, Assessment of Geopressured-Geothermal Resources in the Northern Gulf of Mexico Basin: USGS Circular 790 (op cit), p. 132–155.
- Wassel, R., 2012, Lessons from the Macondo well blowout in the Gulf of Mexico: The Bridge-National Academy of Engineering, v. 42, no. 3, p. 46–53.